Research Square

Preprints are preliminary reports that have not undergone peer review.
They should not be considered conclusive, used to inform clinical practice,
or referenced by the media as validated information.

Observational source choice outweighs the emission scenario in projected dependable precipitation: evidence from 44 rain gauges in southern Brazil

Willyan Júnior Adorian Bandeira
willyan.bandeira@acad.ufsm.br
Universidade Federal de Santa Maria
João Joel Ziotti
Universidade Regional do Noroeste do Estado do Rio Grande do Sul
Ivan Ricardo Carvalho
Universidade Regional do Noroeste do Estado do Rio Grande do Sul
Alessandro Dal'Col Lúcio
Universidade Federal de Santa Maria

Research Article

Keywords: Markov chain, Gamma distribution, NEX-GDDP-CMIP6, Natural variability, Uncertainty partitioning, Rainfed agriculture

Posted Date: November 12th, 2026

DOI: https://doi.org/10.21203/rs.3.rs-11442487/v1

License: This work is licensed under a Creative Commons Attribution 4.0 International License.
Read Full License

Additional Declarations: No competing interests reported.

Observational source choice outweighs the emission scenario in projected dependable precipitation: evidence from 44 rain gauges in southern Brazil

Willyan Júnior Adorian Bandeira[1*], João Joel Ziotti[2], Ivan Ricardo Carvalho[2], Alessandro Dal'Col Lúcio[1]

[1]Departamento de Fitotecnia, Universidade Federal de Santa Maria, Santa Maria, Brazil.

[2]Universidade Regional do Noroeste do Estado do Rio Grande do Sul, Ijuí, Brazil.

[*]**Corresponding author:** willyan.bandeira@acad.ufsm.br

ORCID: Willyan Júnior Adorian Bandeira [https://orcid.org/0000-0002-9430-3664], Ivan Ricardo Carvalho [https://orcid.org/0000-0001-7947-4900], Alessandro Dal'Col Lúcio [https://orcid.org/0000-0003-0761-4200]

Abstract

Dependable precipitation, defined as a lower quantile of the distribution of monthly totals, is the quantity that guides irrigation design and the definition of sowing windows, yet it is seldom projected for future conditions. This study assembled five precipitation datasets over 44 sites in northwestern Rio Grande do Sul, Brazil, from 2002 to 2025, fitted an occurrence-intensity model for each site, dataset and month, and applied change factors derived from five NEX-GDDP-CMIP6 models under three shared socioeconomic pathways and two future windows. The datasets agree on annual volume, with a range of 12% between the highest and the lowest, and disagree on the daily structure that produces it, with 23.8% of wet days at 22.3 mm in the rain gauge network against 38.9% at 11.8 mm in the reanalysis. Across 9504 combinations of site, month and dataset, no projected change exceeded the natural variability band, the maximum signal-to-noise ratio being 0.831 and a signal 4.5 to 10.5 times larger being required for detection. The variance partition assigned 68.9% to 77.6% to natural variability, 12.7% to 18.8% to model choice and 1.5% to 1.9% to the emission pathway. For the absolute value that the end user applies, dataset choice accounted for 6.57% of the variance against 1.51%, a ratio of approximately 4.4 times.

Keywords: Markov chain; Gamma distribution; NEX-GDDP-CMIP6; Natural variability; Uncertainty partitioning; Rainfed agriculture

1 Introduction

Agricultural planning sizes irrigation, reservoirs and sowing windows against the depth exceeded in most years, and not against the mean. This quantity, dependable precipitation, is a lower quantile of the distribution of accumulated totals, conventionally at the 75% and 90% exceedance probability levels, and the gamma distribution is its usual statistical formulation (Thom, 1958). It differs from the extreme value and heavy rainfall tradition (Gumbel, 1958; Chow, 1964), which describes the upper tail and guides drainage and containment works, whereas dependable precipitation answers how much can be counted on. It is a quantity in current use in crop planning and irrigation design, both in Brazil (Silva et al., 2007; Ávila et al., 2009; Coan et al., 2014; Silva et al., 2021; Abreu et al., 2023) and in other rainfed agricultural regions (Mandal et al., 2015; Ucar et al., 2023). Because it depends on a quantile and not on a mean, it is determined by the entire distribution of totals, that is, by the frequency of wet days, by the intensity on those days and by the persistence between them.

CMIP6 projections for South America have been extensively evaluated in recent years. Silva et al. (2026) compared seventeen models against reanalysis in five sub-regions of the continent, Reboita et al. (2024) extended the evaluation to fifty models and five sub-domains, among them the La Plata Basin, which contains the area of this study, and Ferreira et al. (2023) extended the analysis to statistically downscaled precipitation and to drought indices. For southeastern South America the projected net change is positive, yet Almazroui et al. (2021) reported that it remains within the variability of the reference period by mid-century under all scenarios. None of these statistics delivers a dependable value. A reported change in the mean does not indicate which component of precipitation moved, and the two may move in opposite directions, since in Brazil the projected change in rainfall events is governed by frequency and not by intensity (Ballarin et al., 2024) and daily precipitation is strongly uneven, with the change concentrated in a few days of the year (Pendergrass and Knutti, 2018). The decomposition that separates these components is the occurrence-intensity one, classically formulated as a first-order Markov chain for occurrence (Gabriel and Neumann, 1962; Katz, 1977), whose appropriate order varies among climatic regimes (Wilson Kemsley et al., 2021), and as a gamma distribution for wet-day amounts, because it captures the positive skewness typical of daily precipitation (Thom, 1958; Chen and Brissette, 2014). The Markov-gamma pair reproduces frequency, persistence and the

distribution of intensities simultaneously (Verdin et al., 2018), and the perturbation of its parameters by factors derived from climate models, established by Wilks (1992), is the mechanism adopted in this work.

A projected change only acquires meaning when it is large enough to emerge from the natural variability of the quantity itself. Internal climate variability can generate apparent short-term trends larger or smaller than the long-term forced trend, which hinders detection of the anthropogenic signal at local and regional scales (Martel et al., 2018) and accounts for a relevant share of the uncertainty in precipitation projections (Deser et al., 2012; Lehner et al., 2020). The time of emergence concept formalizes this condition by identifying the moment at which the change becomes detectable against background variability (Gampe et al., 2024), and responses to forcing may remain statistically undetected for decades (Samset et al., 2020). Quantifying this condition requires an explicit variability reference. Sun et al. (2018) derived the band within which a difference between the means of two windows is indistinguishable from the sampling variability of the climate itself, and Hawkins and Sutton (2009) established the partition of projection uncertainty among model, emission scenario and internal variability.

Although change factors are derived from models, the historical baseline and the variability band come from observations, so that the projected value in absolute terms depends on the observational source adopted. Rain gauge networks, satellite products and reanalyses disagree on the mean, on interannual variability and on the frequency of extreme events, especially in regions of low station density (Prein and Gobiet, 2017; Tarek et al., 2021). These divergences influence model evaluation, bias correction and the resulting projections (Gampe et al., 2019; Casanueva et al., 2020; Pathak et al., 2023), and propagate as far as estimates of agricultural response to climate (Parkes et al., 2019). For dependable precipitation in particular, Pannak et al. (2026) showed that estimates vary with the gridded product adopted, yet the analysis ends in the historical period. The regional literature itself acknowledges the limitation, with Reboita et al. (2024) attributing observational uncertainty in South America to the low density of the surface station network and Almazroui et al. (2021) concluding that multiple observational products should be employed. The uncertainty associated with the observational choice may equal or exceed that associated with the climate models themselves (Tarek et al., 2021). It remains open, however, how this uncertainty

compares with the magnitude of the change signal projected for the quantity that the end user actually applies.

These three lines do not meet in the literature. Dependable precipitation is estimated retrospectively, over observed series (Mandal et al., 2015; Ucar et al., 2023; Pannak et al., 2026), agricultural projections of water availability employ deterministic effective rainfall or quantiles of water demand and not of precipitation (Yoo et al., 2012; Ahmad and Choi, 2021), and the propagation of the observational choice stops at the comparison with model uncertainty, without confrontation with the magnitude of the projected signal. The objective of this study is (i) to quantify how much the observational source alters the occurrence-intensity structure and the resulting dependable precipitation across a network of 44 sites, (ii) to project monthly dependable precipitation under three emission scenarios, SSP1-2.6, SSP2-4.5 and SSP5-8.5, for two future windows, and (iii) to test whether the projected change is detectable against natural variability and to partition the uncertainty among natural variability, model choice, emission scenario and observational source.

2 Materials and Methods

2.1 Study area

The study covers the northwestern region of Rio Grande do Sul, the southernmost state of Brazil, between approximately 27.0º and 29.0º S and 52.4º and 55.4º W (Fig. 1). The regional climate is humid subtropical without a dry season, Cfa type in the Köppen classification (Alvares et al., 2013), with rainfall distributed throughout the year. In the observational network assembled in this study, monthly totals range from about 119 mm in August to about 237 mm in October, with a mean annual total close to 1900 mm. The near absence of a seasonal minimum conditions the evaluation of the models (Section 2.5). The region is dominated by rainfed grain production, chiefly soybean, maize and wheat, so that the quantity relevant to planning is the precipitation that can be counted on in most years, and not the long-term mean.

2.2 Observational data sources

Five independent observational sources were assembled for the period from 2002 to 2025, chosen so that the effect of the observational choice could be isolated at the same geographical points. (I) *Rain gauge network (ANA)* - Daily records from the rain gauge network of the Brazilian

National Water Agency (ANA) were obtained from the HidroWeb system through the 'hydrobr' package for R (Calegario et al., 2026). Stations were selected within the bounding rectangle of the study region, requiring at least 20 years of record with at most 20% of missing days between 2002 and 2025. Forty-five stations met these criteria before quality control. (II) *Satellite-gauge product (CHIRPS)* - Daily rainfall from the Climate Hazards Group InfraRed Precipitation with Station data (CHIRPS), version 2.0, at 0.05º resolution (Funk et al., 2015), was downloaded for the study rectangle and extracted at the coordinates of each site. (III) *Reanalysis (NASA POWER)* - Corrected total daily precipitation (PRECTOTCORR) was obtained from the NASA Prediction of Worldwide Energy Resources service, whose performance under Brazilian conditions was evaluated by Monteiro et al. (2018), through the 'nasapower' package for R (Sparks, 2018), at the coordinates of each site. (IV) *Automatic weather stations (INMET)* - Hourly records from the automatic network of the Brazilian National Institute of Meteorology were obtained from the institute's public archive and aggregated to daily totals. Because the archive reports times in UTC and the region lies in UTC-3, daily aggregation was performed over the local day. A day was retained only when at least 20 of the 24 hourly values were valid. The effect of the day boundary was quantified by aggregating the same records under both calendars. The two series correlated at $r = 0.96$, yet 12.8% of the days differ by more than 1 mm, which is why all comparisons among sources are made at the monthly scale. (V) *Reference rain gauge* - A privately operated rain gauge at Nova Ramada (28º 04' 55.9" S, 53º 39' 30.9" W), read manually each day, provides the longest continuous local record available to the authors and lies 3.0 km from ANA site 2853035. Its archive records only the days on which rain occurred, the remaining days being confirmed dry, so that the calendar was reconstructed with zeros before analysis. Three months with documented collection failures (March and April 2011, December 2013) were flagged as missing and not as zero.

2.3 Quality control and network definition

A single set of methodological procedures was applied to all sources, so that the differences observed could not be attributed to differences in data treatment. A day was classified as wet when the daily total reached 1.0 mm, the conventional threshold of the climate index literature, while thresholds of 0.1 mm and 2.0 mm were retained as a sensitivity analysis. A month entered the analysis only with at least 26 valid days, and a year entered the annual statistics only with at least 90% of the days present. The series were audited for duplicate dates, negative values, daily totals

147 above 300 mm, repeated positive values on consecutive days, dry spells longer than 90 days, spatial
148 coherence with sites less than 50 km away, stationarity by the Mann-Kendall test and absence of a
149 change point by the Pettitt test. Exclusion of a site required concurrent failure in independent
150 criteria, so that no series was discarded on the basis of a single indicator, a criterion adopted to
151 avoid mistaking local variability for sensor malfunction. Site 2854016 of the ANA network met
152 this condition and was excluded (Online Resource 1, Section S1). The retained network comprises
153 44 sites.

154 Stations from the remaining point sources were associated with the nearest ANA site, and
155 one automatic station more than 30 km from any site was discarded, because at that separation the
156 disagreement reflects spatial distance and not the measurement source. Nine automatic stations
157 were retained, at separations of 1.1 to 27.5 km. The resulting design is nested, with three sources
158 (ANA, CHIRPS and NASA POWER) at the 44 sites and four sources at nine of them. A single
159 daily total above the audit threshold was retained, because it corresponds to the May 2024 flood
160 event in Rio Grande do Sul and is confirmed at neighbouring sites and in the remaining sources on
161 the same date.

162 **2.4 Climate model data**

163 Daily precipitation was obtained from NEX-GDDP-CMIP6, the NASA Earth Exchange
164 Global Daily Downscaled Projections dataset (Thrasher et al., 2022), which applies bias correction
165 and spatial disaggregation to CMIP6 output on a 0.25º grid. Because it is already bias corrected,
166 the product is treated here as statistically downscaled and corrected output, and not as raw model
167 output. Six models were used, all with the 'r1i1p1f1' member: ACCESS-CM2, ACCESS-ESM1-
168 5, INM-CM4-8, INM-CM5-0, IPSL-CM6A-LR and KACE-1-0-G. Seven windows were extracted
169 at the coordinates of each network site, the historical window being 1985 to 2014, and two future
170 windows, 2027 to 2040 and 2041 to 2070, under each of three emission scenarios, SSP1-2.6, SSP2-
171 4.5 and SSP5-8.5. The three scenarios span the plausible range of radiative forcing in 2100, from
172 2.6 to 8.5 W m^{-2}, which allows the effect of the emission pathway to be separated from the effect
173 of internal variability. KACE-1-0-G, excluded from the ensemble for the reasons given in Section
174 2.5, was extracted for the historical window and for the two SSP2-4.5 windows, but takes part in
175 no result reported here.

Two features of the source data required explicit treatment. First, precipitation is stored as a flux in kg m^{-2} s^{-1} and was converted to mm day^{-1} by multiplying by 86400. Second, the models use different calendars. KACE-1-0-G uses a 360-day calendar, with twelve months of 30 days. Mapping these dates onto the Gregorian calendar produces 53 collisions. The month was therefore reconstructed from the position of each record within the year, and not from the converted date, which is exact for a 360-day calendar and preserves every record. Ignoring this displaces about 10 mm per month between February and March in that model. The 360-day calendar also gives KACE-1-0-G annual totals about 1.4% lower in absolute terms, which cancels in the change factor because the two windows share the calendar. All files were audited before analysis for completeness, duplicate dates, unit conversion and plausibility of annual totals.

2.5 Model evaluation and ensemble selection

The models were evaluated against the observed annual cycle of the 44-site network for the period from 2002 to 2014, the overlap between the CMIP6 historical simulation and the observational network. Simulated and observed monthly climatologies were compared by RMSE, mean bias, Willmott's index of agreement d (Willmott, 1981), Nash-Sutcliffe efficiency (NSE), Pearson correlation and Kling-Gupta efficiency (KGE; Gupta et al., 2009), reported in Section 3.3. RMSE was adopted as the primary criterion. The regional annual cycle has small amplitude, and over twelve points of a signal of this nature the correlation is unstable, so that models of similar error receive very different correlations without the difference corresponding to distinct physical performance.

One model, KACE-1-0-G, was excluded from the ensemble because of a phase error, and not because of error magnitude. Its annual cycle is inverted with respect to the observations, peaking in May rather than in October, the month of the observed maximum. The exclusion follows from the nature of the change factor method, since the ratio between two windows of the same model cancels a level bias but does not correct an inverted cycle, because the ratio for each month then describes the dynamics of the wrong month. As KACE-1-0-G is the only model in the set with a 360-day calendar, the hypothesis that the inversion was an artefact of the month reconstruction was tested by recomputing the climatology under three independent criteria of month assignment. All three return a negative correlation with the observed annual cycle at zero shift, from -0.184 to -0.185, and the same optimal circular shift of seven months, at which the correlation reaches only

206 0.59 to 0.61. The five retained models require no shift under any criterion. A calendar artefact
207 would have been removed by one of the criteria or recovered by the shift, and neither occurs
208 (Online Resource 1, Section S2). The five remaining models compose the ensemble, and the
209 evaluation is reported for all six, so that the criterion can be verified.

210 The exclusion is convergent with independent evaluations. KACE-1-0-G has been
211 classified as of low skill for precipitation and removed from multi-model ensembles in other
212 regions (Kazora et al., 2025; Talukder et al., 2025), and was identified as an outlier in the monthly
213 precipitation climatology of NEX-GDDP-CMIP6 itself (Prasetya et al., 2026). Seasonal cycle
214 biases over southeastern South America are documented for the Unified Model family, to which
215 KACE-1-0-G belongs, with overestimation of precipitation in that sector (García-Franco et al.,
216 2020). For Brazil, Firpo et al. (2022) placed ACCESS-ESM1-5, IPSL-CM6A-LR and INM-CM4-
217 8 among the models of highest skill for monthly rainfall, three of the five retained here. Following
218 Maraun et al. (2017), models whose temporal structure of precipitation is fundamentally
219 misrepresented should be discarded before the application of statistical corrections, and not
220 corrected by them. It should be noted that the performance of KACE-1-0-G varies strongly among
221 regions, so that the exclusion here is regional and not a general judgement on the model.

222 **2.6 Occurrence-intensity model**

223 Dependable precipitation was obtained from a two-part model, fitted separately for each
224 site, source and calendar month. Occurrence was described by a first-order Markov chain, with
225 state *J* equal to 1 on a wet day and to 0 on a dry day, defined by the transition probabilities.

226 $$p_{01} = \Pr(J_t = 1 \mid J_{t-1} = 0), \quad p_{11} = \Pr(J_t = 1 \mid J_{t-1} = 1) \qquad (1)$$

227 Transitions were counted only between consecutive days of the same month, and the chain
228 was compared with an independent Bernoulli model by the Akaike information criterion. The
229 marginal probability of a wet day implied by the chain is

230 $$\pi = \frac{p_{01}}{1 + p_{01} - p_{11}} \qquad (2)$$

231 Wet-day intensity was described by a gamma distribution with shape parameter α and rate
232 parameter β, fitted by maximum likelihood and requiring at least 30 wet days in the combination,

$$f(x \mid \alpha, \beta) = \frac{\beta^{\alpha}}{\Gamma(\alpha)} x^{\alpha-1} e^{-\beta x}, \quad x > 0 \tag{3}$$

whose mean and coefficient of variation are

$$\mathrm{E}[X] = \frac{\alpha}{\beta}, \quad \mathrm{CV}[X] = \frac{1}{\sqrt{\alpha}} \tag{4}$$

Equation (4) links the shape of the daily distribution to the lower quantile that defines dependable precipitation, because larger shapes produce less variable daily intensity, more concentrated monthly totals and a higher lower quantile. The gamma was retained in every month. Across the 1584 combinations of site, source and month, it was favoured by AIC in 58.1% and lay within 2 AIC of the best-fitting family in 84.6%, when the left truncation imposed by the 1.0 mm wet-day threshold is accounted for in the likelihood. Fitting the same families without that correction reverses the ranking in favour of the lognormal, which illustrates that the comparison is sensitive to the treatment of the threshold rather than to the families themselves. The gamma also has the property that a sum of independent variates of equal rate is itself gamma, which is what makes Eq. (8) exact. Replacing it by the family favoured by AIC shifts monthly dependable precipitation by a median of 3.8 mm, about one tenth of the natural variability band, and does not alter the projected change, because the change factor is applied identically (Online Resource 1, Section S4).

2.7 Change factors

The projections were applied by means of change factors, and not by direct use of the model output. For each site, model, month and future window, two factors were computed as ratios between the future window and the historical window of the same model

$$f_{\mathrm{occ}} = \frac{\pi_{\mathrm{fut}}}{\pi_{\mathrm{hist}}}, \quad f_{\mathrm{int}} = \frac{\bar{I}_{\mathrm{fut}}}{\bar{I}_{\mathrm{hist}}} \tag{5}$$

where π is the simulated frequency of wet days and $\bar{I}$ the simulated mean intensity on wet days. The ratio between two windows of the same model cancels its level bias. The historical window of the factors is the full period from 1985 to 2014, independent of the evaluation window of Section 2.5, because the computation of a change factor involves no observation. A single grid cell serves all observational sources of a given site, so that the change factor is identical across

sources. This choice is deliberate, as it confines the effect of the observational source to the baseline, the only condition under which it can be isolated.

2.8 Projection of dependable precipitation

The factors were applied to the observed baseline parameters and monthly totals were resimulated by Monte Carlo with 10,000 replicates for each combination of site, source, model, month and window, from random seed 42. The intensity factor scales the gamma mean while holding the shape fixed, so that only the rate parameter moves.

$$\alpha^* = \alpha, \quad \beta^* = \frac{\beta}{f_{\mathrm{int}}} \tag{6}$$

The occurrence factor requires distinct treatment. By Eq. (2), π is not proportional to p01 and p11, so that multiplying the two transition probabilities by a factor does not multiply π by that same factor. The occurrence factor was applied as a common shift in the logits of the two probabilities, solving numerically for the constant c that satisfies

$$\mathrm{logit}\left(p_{1\mathrm{j}}{}^*\right) = \mathrm{logit}\left(p_{1\mathrm{j}}\right) + \mathrm{c}, \quad \mathrm{j} = 0, 1, \quad \text{with c such that} \quad \pi^* = f_{\mathrm{occ}}\pi \tag{7}$$

A common shift in the two logits preserves the odds ratio between p11 and p01, so that persistence remains unchanged and only the frequency moves. Each replicate simulates the occurrence chain over the days of the month from the stationary distribution, counts the K wet days and obtains the monthly total S in a single step, by the property that the sum of k independent gamma variables of the same rate is itself gamma,

$$S = \sum_{i=1}^{K} X_i, \quad S \mid \mathrm{K} = \mathrm{k} \sim \mathrm{Gamma}(k\alpha, \beta^*) \tag{8}$$

The procedure is exact and dispenses with day-by-day simulation of the intensities. Dependable precipitation was then read from the empirical distribution function of the simulated monthly totals, F with subscript S, as

$$\mathrm{PP}_{75} = F_S{}^{-1}(0.25), \quad \mathrm{PP}_{90} = F_S{}^{-1}(0.10) \tag{9}$$

The baseline value was obtained by the same procedure with both factors equal to one, so that the baseline and the projection carry the same Monte Carlo error.

2.9 Natural variability and detectability

The projected change was tested against the sampling variability of the climate itself. Following Sun et al. (2018), the band within which a difference between the means of two windows is indistinguishable from natural variability is

$$\Delta P_{0.9} = 1.64\,\sigma\sqrt{\frac{1}{n_1} + \frac{1}{n_2}} \tag{10}$$

where σ is the interannual standard deviation of the monthly total at that site and source, n_1 the number of observed years and n_2 the length of the future window. The band was computed per site, source and month, and combinations with fewer than ten usable years were excluded from this step. The signal-to-noise ratio of each combination was defined as

$$\mathrm{S/N} = \frac{|\Delta \mathrm{PP}_{75}|}{\Delta P_{0.9}} \tag{11}$$

and the combination was classified as detectable when S/N exceeded unity and at least 80% of the ensemble members agreed on the sign of the change, as dominated by inter-model uncertainty when the band was exceeded without that agreement, and as within natural variability in the remaining cases. The band of Sun et al. (2018) was derived for a difference of means and is applied here to a quantile, so that the comparison is one of order of magnitude and not a formal identity. Two auxiliary quantities describe the distance to detection, the first being the factor by which the projected change would have to grow to reach the band and the second the fraction of cases that would be detectable in the limit of an infinitely long observed record, a situation in which the band reduces to $\frac{1.64\,\sigma}{\sqrt{n_2}}$.

2.10 Uncertainty partitioning

The contributions to the uncertainty of the projected quantities were separated following the logic of Hawkins and Sutton (2009), which accounts for three axes, model, emission scenario and internal variability, with the addition of a fourth axis seldom considered, the observational source that defines the baseline. For each site, month and period, the forty-five projected values y arising from the crossing of I = 3 sources, J = 5 models and K = 3 scenarios decompose exactly, in a balanced design, as

$$y_{ijk} = \overline{y} + a_i + b_j + d_k + e_{ijk} \tag{12}$$

where the bar over y denotes the mean of the forty-five values of the cell, a_i is the main effect of the observational source, b_j that of the model, d_k that of the emission scenario and e_{ijk} the interaction residual. Each main effect is the deviation of the corresponding marginal mean from the overall mean, and the residual is obtained by difference, so that the three effects sum to zero. The variances associated with each axis are

$$V_{\mathrm{F}} = \frac{1}{I}\sum_i a_i{}^2, \quad V_{\mathrm{M}} = \frac{1}{J}\sum_j b_j{}^2, \quad V_{\mathrm{C}} = \frac{1}{K}\sum_k d_k{}^2, \quad V_{\mathrm{I}} = \frac{1}{IJK}\sum_{ijk} e_{ijk}{}^2 \qquad (13)$$

These four components sum exactly to the variance of the forty-five values, because in a balanced design the main effects are orthogonal to one another and to the residual. Natural variability does not enter this decomposition and enters as an independent fifth component in the total over which the percentage shares are computed, with c running over the five components,

$$V_{\mathrm{N}} = \sigma^2\left(\frac{1}{n_1} + \frac{1}{n_2}\right), \quad F_c = 100\,\frac{V_c}{\sum_{c'} V_{c'}} \qquad (14)$$

The natural variability component is the variance expressed by the band of Section 2.9. The period does not enter as a factor, because the two windows have different lengths and therefore different bands, so that the partition was computed separately within each one. The components were summarized by the mean across sites, and not by the median, because the shares sum to one hundred per cent in each cell and the mean, being linear, preserves that sum. The partition was computed twice, once for the projected change and once for the projected level. As the level is the sum of the baseline and the change, and the baseline depends only on the source, the model, scenario and interaction terms are identical in the two partitions, only the source term differing between them, and it is this contrast that constitutes the result. Robustness with respect to ensemble composition was assessed by recomputing the median with each model removed in turn.

2.11 Software

All processing and analysis were carried out in R version 4.6.1. Wet-day intensity distributions were fitted by maximum likelihood with ‘fitdistrplus’ version 1.2.6 (Delignette-Muller and Dutang, 2015), the Mann-Kendall and Pettitt tests used ‘trend’ version 1.1.8 (Pohlert, 2026), raster and vector operations used ‘terra’ and ‘sf’, and the figures were produced with ‘ggplot2’, ‘ggridges’, ‘patchwork’ and ‘ggspatial’. The analysis scripts, the observational series

and the NEX-GDDP-CMIP6 point extract are deposited together in a public repository (Bandeira et al. 2026), which reproduces every table and figure of this article without any external download.

3 Results

3.1 The observational network and its sources

The five observational sources assembled over the same 44 locations agree on the annual volume of rainfall. The mean annual total is 1934 mm in the ANA network, 1920 mm in CHIRPS and 1704 mm in the NASA POWER reanalysis, a range of 12% between the highest and the lowest value, while the INMET automatic stations record 1865 mm and the reference rain gauge 2343 mm (Table 1; Fig. 2). This agreement, however, results from two deviations that offset each other. Decomposing the annual total into the number of wet days and the mean intensity on those days, the ANA network records 87 wet days per year at 22.3 mm each, against 142 days at 11.8 mm in NASA POWER, that is, 63% more wet days and 47% less rainfall on each of them. The product of the two components recomposes the annual total to within 2% in both sources. CHIRPS occupies an intermediate position, with 98 wet days at 19.6 mm.

The disagreement among sources reappears in the tails and in interannual variability (Table 1). The 99th percentile of daily totals is 107.3 mm in the ANA network, 77.1 mm in CHIRPS and 61.1 mm in NASA POWER, so that the reanalysis reduces the extreme daily event to little more than half the value recorded by the rain gauge. The interannual coefficient of variation of the annual total is 22.1% in ANA, against 19.7% in CHIRPS and 19.8% in NASA POWER. This last difference has a direct consequence for the detectability step, because the interannual standard deviation is the term that defines the natural variability band in Eq. (10).

Four of the 44 ANA series show a significant monotonic trend by the Mann-Kendall test and one shows a change point by the Pettitt test, while none of the 44 CHIRPS or NASA POWER series shows a trend or a change point at the same locations (Table 1). The comparison of proportions is not conclusive in isolation (Fisher exact test, $p = 0.116$), but the correlation structure of the Sen slopes is informative, in that the slopes of the two gridded products agree with each other ($r = 0.480$) and do not agree with those of the rain gauges ($r = -0.126$ against CHIRPS and $r = -0.141$ against NASA POWER). The magnitude reinforces the interpretation, as the largest Sen slope of the ANA network, +66.3 mm per year, would correspond over two decades to an increment

close to the annual total of the region, while at the same point the two gridded products record +1.6 and -12.0 mm per year. Trends of this magnitude at isolated sensors, not reproduced by any independent product, are consistent with station inhomogeneity. The network was therefore treated as stationary.

3.2 Occurrence-intensity structure

The first-order Markov chain outperformed the independent Bernoulli model by AIC in all 1704 combinations of site, source and month, without exception. The median AIC difference is 42.6 in the ANA network, ranging from 34.0 in August to 65.5 in May (Table 2). This variation is not random, in that the months of greatest gain are those of greatest persistence, measured by the difference between p11 and p01, which reaches 0.254 in May and 0.225 in March. The advantage of the chain over the independent model is largest exactly where the clustering of wet days is largest, which constitutes an internal check on the fit.

The monthly parameters of the ANA network describe an annual cycle in which occurrence and intensity move in the same direction (Table 2; Fig. 3a). The marginal probability of a wet day ranges from 0.192 in August to 0.297 in October and the mean wet-day intensity ranges from 17.2 mm in February to 25.7 mm in October. October is the maximum in both components and August the minimum in both, which explains the pronounced peak and trough of the observed annual cycle. Persistence follows a distinct pattern, being lowest in October (0.146), precisely the month of greatest frequency, and highest in May (0.254). Rain falls more often in October, yet in less clustered events, whereas in May it falls fewer times and in longer sequences. The shape of the gamma distribution remains close to unity throughout the year, between 0.954 and 1.202, which indicates an approximately exponential daily intensity.

The contrast among sources is larger than the contrast among months (Table 3). The marginal probability of a wet day is 0.234 in the ANA network, 0.264 in CHIRPS and 0.385 in NASA POWER, and the corresponding mean intensities are 21.7, 19.5 and 12.1 mm. In the frequency-intensity plane (Fig. 3b), the three sources occupy disjoint regions along a decreasing relation, and the separation between the clouds exceeds the internal scatter of each one. Persistence follows the same ordering, from 0.193 in ANA to 0.371 in NASA POWER, and the advantage of the Markov chain grows in the same direction, from 42.6 to 118.6 of AIC difference. The reanalysis not only distributes the same rainfall over more days, but also produces longer wet sequences.

The parameter that most governs dependable precipitation is not the mean, but the shape of the gamma distribution (Table 3). CHIRPS presents a shape of 1.727, against 1.102 in ANA and 1.082 in NASA POWER. By Eq. (4), the coefficient of variation of daily intensity is the inverse of the square root of the shape, so that CHIRPS rainfall is less variable from one wet day to the next, with a coefficient of variation of 0.76 against 0.95 and 0.96 in the remaining sources. Monthly totals composed of less variable events have a narrower distribution, and narrower distributions have a higher lower quantile. This is why CHIRPS yields the highest monthly dependable precipitation of the set, 104.8 mm, against 95.5 mm in the ANA network and 95.7 mm in NASA POWER, despite presenting an annual total lower than that of the rain gauge network.

Aggregated to the year, the spread among the three sources present at all locations reaches 11.9% of 75% dependable precipitation, as a median across the 44 sites, ranging from 5.3% to 25.3% depending on the location (Fig. 3c). Two studies conducted at the same site, over the same period and with the same method, differing only in the observational source adopted, would therefore arrive at dependable values differing by more than one tenth, and by one quarter in the most extreme cases.

3.3 Model performance and ensemble selection

The best fit to the observed annual cycle was that of ACCESS-ESM1-5 (RMSE = 14.1 mm; NSE = 0.80; r = 0.97), followed by INM-CM4-8, IPSL-CM6A-LR, ACCESS-CM2 and INM-CM5-0, with RMSE between 20.9 and 28.8 mm and r between 0.52 and 0.79 (Table 4; Fig. 4). The five retained models cover a wide range of performance, from NSE 0.80 to 0.15, and that range is part of the uncertainty reported below. KACE-1-0-G separates from the set by a distinct order of magnitude of error, with an RMSE of 61.5 mm, more than twice that of the model immediately preceding it, and an NSE of -2.890, that is, the observed mean would reproduce the annual cycle better than this model. The negative correlation with the observed cycle (r = -0.185) identifies the nature of the problem, which is not one of amplitude error but of phase, with a simulated peak in May against an observed peak in October (Fig. 4), and the model was accordingly excluded from the ensemble.

3.4 Projected change factors

The change factors remain close to 1.00 in the three scenarios and in the two future windows, with values between 0.69 and 1.25 (Fig. 5). The set shows no systematic ordering along either axis. Between horizons, the 2027-2040 window frequently presents factors similar to or larger than those of the 2041-2070 window. Between scenarios, the ordering expected from the increase in radiative forcing is not consistently reproduced. The largest reductions concentrate in winter months and in specific models, and the largest increases occur sporadically in spring and summer. The absence of systematic ordering constitutes the first indication that the projected signal lies below the noise floor associated with variability among models, months and scenarios.

3.5 Projected dependable precipitation

Fig. 6 brings together, in four spatial views of the same window and the same scenario (SSP2-4.5, 2041-2070), the quantities that support the argument of the study. The observed baseline of the ANA network, expressed as the sum of the twelve monthly values of 75% dependable precipitation, ranges from 1011 to 1333 mm across sites, with a median of 1181 mm, and increases from west to east (Fig. 6a). The relative range among ANA, CHIRPS and NASA POWER at the same point has a median of 11.9% and a range of 5.3% to 25.3%, with a gradient inverted with respect to that of the baseline and the largest disagreements at the western end of the network (Fig. 6b). The projected change in the same annual quantity is positive at all 44 sites, from +18.8 to +70.2 mm, with a median of +45.0 mm, equivalent to 3.7% of the baseline (Fig. 6c). The signal-to-noise ratio, taken at each site in the month of highest ratio, that is, in the most favourable case that site offers, ranges from 0.212 to 0.772, with a median of 0.359, and no site reaches the reference circle representing unit ratio (Fig. 6d).

The joint reading of panels (b) and (c) of Fig. 6 is the central result of the figure. At all 44 sites, without exception, the range among observational sources exceeds the projected change when both are expressed on the same relative scale, with medians of 11.9% against 3.7%, a ratio of approximately three times. As the spatial gradients of the two quantities point in opposite directions, the contrast is most marked in the western sector of the network, where the projected signal is smaller and the disagreement among sources is larger.

Fig. 7 confronts projected dependable precipitation with the baseline in the three observational sources. The grey band represents the range among the five retained models, from 19 mm in February to 53 mm in May, and the three emission pathways remain contained within it

in every month and in every source, with a separation between scenarios rarely greater than 15 mm. The ordering among scenarios does not follow radiative forcing, since in October SSP2-4.5 projects a reduction of 1.3 mm while SSP1-2.6 projects an increase of 18.8 mm. The only months in which the three scenarios agree in direction and magnitude are April, from +8.5 to +13.9 mm, and June, from +7.3 to +11.4 mm. The decisive contrast, however, lies between the panels and not within them. The baseline sums 1183 mm in the ANA network, 1279 mm in CHIRPS and 1162 mm in NASA POWER, so that changing the observational source displaces the curve more than changing the emission scenario.

3.6 Detectability and uncertainty partitioning

Month by month, under SSP2-4.5 and 2041-2070 on the ANA baseline, the projected change in 75% dependable precipitation ranges from -5.2 mm in August to +18.0 mm in November, against a natural variability band ranging from 29.1 mm in August to 60.3 mm in December (Table 5). The resulting signal-to-noise ratio lies between 0.027 in October and 0.343 in November, so that no month approaches unity (Fig. 8a). November, the month of largest absolute change, reaches little more than one third of the threshold. Agreement among the five models on the sign of the change is 0.6 in nine of the twelve months, that is, three models against two, so that the second detectability condition would not be satisfied either, had the first been. All twelve months were classified as within natural variability.

The variance partition assigns the largest share of the uncertainty to natural variability, from 68.9% to 77.6% depending on the quantity and the period (Table 6; Fig. 8b). Model choice accounts for 12.7% to 18.8% and the emission scenario for 1.5% to 1.9%, a share that decreases from the near window to the distant one because the variance among models grows faster than the variance among scenarios. The interaction term remains between 5.4% and 7.2%, which indicates that the additive decomposition describes the structure of the data well. The observational source behaves differently according to the quantity, accounting for 0.06% and 0.10% of the variance of the projected change, because the change factor is identical across sources, and for 4.52% and 6.57% of the variance of the projected level, which is the quantity the end user applies. For the level in 2041-2070, the choice of observational source weighs approximately 4.4 times more than the choice of emission scenario, 6.57% against 1.51%.

The result depends neither on the emission scenario nor on the horizon considered (Table 7; Fig. 9). Across the 9504 combinations of site, month and source evaluated, corresponding to 1584 cases in each of the six combinations of scenario and window, no case was classified as detectable. The median signal-to-noise ratio ranges from 0.098 under SSP2-4.5 in 2041-2070 to 0.216 under SSP5-8.5 in the same period, the 90th percentile remains between 0.320 and 0.446, and the largest value observed across the whole network is 0.831, under SSP5-8.5 in 2041-2070. The projected change would have to be 4.5 to 10.5 times larger, depending on the scenario and the window, to reach the band. The median band is 48.6 mm in the 2027-2040 window and 39.8 mm in the 2041-2070 window, identical across scenarios within each window, because it depends only on the observed series and on the length of the future window.

Three checks support the robustness of the non-detection. The first shows that the conclusion does not depend on any particular model. Recomputing the ensemble median with each model removed in turn, the median ratio remains between 0.075 and 0.302, and in 34 of the 36 combinations of removed model, scenario and window no case exceeds the band, while in the two remaining ones the exceeding fraction is 0.06%, equivalent to one case in 1584. The second shows that the result does not follow from the length of the observed record. In the limit of an infinitely long record, in which the band shrinks by 29.6% as a median, the fraction of detectable cases would rise from zero to only 0.28%, with a maximum of 1.20% under SSP5-8.5 in 2041-2070. The third examines the agreement among models on the sign of the change, whose median is 0.60 across the whole network, with only 40.2% of cases reaching the threshold of 0.80, so that most combinations would fail the second detectability criterion as well.

4 Discussion

Selecting a subset of models is common practice in projection studies, because it is rarely feasible to consider the whole available ensemble. What this work shows is that, for monthly dependable precipitation, the methodological decision of greatest consequence is not that one, but the choice of the observational base on which the projections are applied.

4.1 The disagreement among observational sources is structural

The five sources assembled over the same 44 locations agree on the annual volume, with a range of 12% between the highest and the lowest total, and disagree on the daily structure that

produces that volume. The ANA network records 87 wet days per year at 22.3 mm each and NASA POWER records 142 days at 11.8 mm, with recomposition of the annual total to within 2% in both. The importance of the choice of precipitation dataset had already been established at the global scale by Beck et al. (2017), who evaluated 22 products against 76,086 rain gauges and found marked differences in accuracy and in space-time pattern. The present result adds that, at the daily scale and over a dense network, the disagreement is not expressed in the total but in the partitioning between frequency and intensity, which are precisely the two components that the occurrence-intensity model separates.

The performance of CHIRPS observed in this study finds a direct counterpart in the validation literature. Paredes-Trejo et al. (2017) reported, in northeastern Brazil, that CHIRPS correlates well with the observations but tends to overestimate low values and to underestimate high values of monthly rainfall, with low wet-day detection skill. A distribution that compresses both tails towards the centre is, by definition, a less variable distribution, and in the gamma fit this corresponds to a larger shape parameter. The shape of 1.727 obtained for CHIRPS, against 1.102 in the ANA network, is the parametric expression of that same behaviour, and it is what explains why CHIRPS yields the highest monthly dependable precipitation of the set, 104.8 mm, despite presenting an annual total lower than that of the rain gauge network. Salio et al. (2015) observed in southern South America that products incorporating microwave observations tend to overestimate extreme values above 70 mm, an effect they describe as particularly evident in southern Brazil.

The departure of NASA POWER also finds regional support. Monteiro et al. (2018) evaluated the product under Brazilian conditions and reported a relative error within ±10% in most grid cells, with an explicit exception for southern Brazil. Duarte and Sentelhas (2020) found poorer performance of NASA POWER compared with an interpolated surface dataset for the same agricultural purpose. Nogueira et al. (2018) reported overestimation of rainfall by Eta, TRMM and CHIRPS in Minas Gerais. The body of these evaluations converges with the result obtained here, with the difference that they describe the deviation in terms of totals or of mean error, whereas the decomposition into occurrence and intensity locates its origin. No validation of CHIRPS against stations specifically in Rio Grande do Sul was located, so that the 44-site network assembled here fills a gap in coverage.

4.2 The observational source outweighs the emission scenario

For the projected level in 2041-2070, the observational source accounts for 6.57% of the variance and the emission scenario for 1.51%, a ratio of approximately 4.4 times. Tarek et al. (2021) reached a conclusion of the same nature when evaluating nine precipitation datasets over 1145 African catchments, finding that the uncertainty associated with the reference dataset was equal to or greater than that associated with the climate models for most streamflow metrics. The authors observed that apparently small differences among datasets over the same reference period can propagate and generate large uncertainty in the projections. The present work extends that result in two respects. First, the quantity evaluated is a lower quantile of the distribution of monthly totals, and not a streamflow metric derived from a hydrological model. Second, the comparison is made against the emission scenario, and not against model choice.

The distinction between projected level and projected change is essential to the correct reading of this result. In the projected change, the observational source accounts for 0.06% and 0.10% of the variance, because the change factor is identical across sources by construction. It is in the level, obtained by applying that factor to a baseline that depends on the source, that the effect is expressed, and it is the level that the end user applies. Casanueva et al. (2020) found an analogous sensitivity to the reference dataset in bias adjustment methods, and reported that this sensitivity is greatest precisely for precipitation intensity, dry spell duration and extreme indices, which are the structural quantities decomposed here. Gampe et al. (2019) found a strong influence of the choice of reference dataset on future precipitation projections, above all of extremes, although they also reported a small influence on the signal after bias correction.

The practical consequence of this uncertainty has already been demonstrated in earlier studies. Parkes et al. (2019) showed that gridded weather datasets diverge in their representation of historical temperature and precipitation patterns in India and that these differences generate large uncertainty in estimates of agricultural yield response. The present result sits one step earlier in that chain, in the climatic quantity that feeds the design, and shows that the uncertainty is already in place before any crop model is invoked.

4.3 The projected signal does not emerge from natural variability

Across the 9504 combinations of site, month and source evaluated under three scenarios and two windows, none was classified as detectable, and the largest signal-to-noise ratio of the whole network was 0.831. This result is convergent with Almazroui et al. (2021), who projected an increase in precipitation over southeastern South America under the four SSP scenarios evaluated and reported that most of these changes remain within the variability range of the reference period. The convergence is relevant because the two works reach it by distinct routes, one by comparison with the variability of the reference period at the sub-regional scale and the other by a threshold derived from the standard error of a difference between means, applied site by site.

The comparison with Martel et al. (2018) requires greater caution and reveals a divergence that deserves to be highlighted. Those authors concluded, from two large ensembles, that natural climate variability dominates the uncertainty of extreme precipitation at the local scale until the end of the century, but that for annual and seasonal total precipitation the change signal can be reliably detected even at the local scale. The quantity analysed here is neither of the two. It is a lower quantile of the distribution of monthly totals, which responds to frequency, intensity and persistence simultaneously. The non-detection obtained in this study suggests that the detectability of lower quantiles is closer to the behaviour documented for extremes than to the behaviour documented for totals, which constitutes a hypothesis to be tested in other regions before being generalized.

The treatment of the baseline as stationary is consistent with Sun et al. (2018), who found, in a global dataset of annual precipitation from 1940 to 2009, that the changes in most cells, 84% of them, lie within the plausible bounds of no significant change at the 90% level. The persistence of the non-detection across scenarios also finds a parallel in Samset et al. (2020), who showed that the response to changes in forcing may take decades to become discernible. Deser et al. (2012) estimated that internal variability accounts for at least half of the spread among models in projected trends up to 2060, a magnitude consistent with the share of 68.9% to 77.6% attributed here to natural variability. The time of emergence framework formalized by Gampe et al. (2024) provides the conceptual basis for a result of this kind.

4.4 Implications for agricultural planning

The median projected change is equivalent to 3.7% of the annual baseline, while the range among observational sources reaches 11.9% in the same aggregate, and this relation holds at all 44

sites. Yoo et al. (2012) obtained a result of remarkably similar magnitude when projecting the design water requirement of irrigated rice in South Korea under three scenarios, with rates of change below 3% in all of them. The coincidence in order of magnitude between two independent studies, on different continents and with different design quantities, reinforces the reading that changes of this magnitude will hardly be separable from interannual noise with the observational records available today.

The practical implication is one of prioritization. Ahmad and Choi (2021) showed, for the rice-wheat system in Pakistan, that increments of effective rainfall did not compensate for the higher water demand because the occurrence of rainfall and the duration of the peak irrigation demand became mismatched, which reiterates that the temporal distribution, and not the volume alone, governs the design. In the dependable precipitation studies conducted in Brazil and elsewhere, the choice of distribution and of source is rarely treated as a quantified source of uncertainty. Abreu et al. (2023) identified the gamma distribution as the most adequate for the monthly total in all twelve months of the year in Mato Grosso do Sul, Coan et al. (2014) employed the gamma at 92 points in Santa Catarina and Ávila et al. (2009) adopted the lognormal in southern Minas Gerais. For the practitioner in the region studied here, the result indicates that methodological attention yields more when directed at the observational base than at the emission pathway.

4.5 Phase error and the limits of ranking indices

The exclusion of KACE-1-0-G from the ensemble illustrates a limitation of the usual model evaluation protocols. Reboita et al. (2024) evaluated 50 CMIP6 models in five sub-regions of South America and ranked KACE-1-0-G among the three best for precipitation in the La Plata Basin, which is the sub-region containing the area of this study. The metrics employed in that ranking were the mean, the standard deviation, the Pearson spatial correlation, the amplitude of the annual cycle and the linear trend. None of them is sensitive to the phase of the annual cycle. The amplitude, defined as the difference between the wettest and the driest month, takes an identical value for a correct cycle and for the same cycle inverted, and the spatial correlation evaluates the geographical pattern and not the ordering of the months. The two results are therefore compatible, and the difference between them indicates that a model can be well ranked by well-defined indices while having the seasonal phase wrong.

The consequence of this limitation depends on the method applied, in that for an evaluation of mean climatology a phase error is partly absorbed by the aggregation. For the change factor method it is not, because the ratio between two windows of the same model cancels the level bias but transports the dynamics of the wrong month to the corresponding month of the baseline. Maraun et al. (2017) argued that bias correction does not overcome structural model errors and that its naive application may produce implausible change signals and poorly informed adaptation decisions, a recommendation that supports the decision to discard the model rather than correct it. The regional evidence converges. Kazora et al. (2025) ranked KACE-1-0-G among the worst performing models for extreme precipitation indices in Central Eastern Africa and Talukder et al. (2025) placed it among the worst performing for precipitation in Bangladesh. These evaluations, together with the one presented here, indicate that model performance varies strongly among regions, so that the exclusion adopted is regional and does not constitute a general judgement on the model.

Two additional points place the result in context. KACE-1-0-G shares the atmospheric component of the Unified Model family, for which García-Franco et al. (2020) documented austral summer biases in the Atlantic Intertropical Convergence Zone, with overestimation of precipitation in southeastern Brazil and underestimation in Amazonia, biases that the authors attribute to Atlantic sea surface temperatures. Furthermore, the bias correction and downscaling applied in NEX-GDDP-CMIP6 did not remove seasonal cycle biases. Prasetya et al. (2026), evaluating 35 models of the same dataset over Indonesia, reported the persistence of systematic biases in the annual cycle, with underestimation of the wet season peak and overestimation of the dry season. Local evaluation therefore remains necessary even over output that has already been corrected.

4.6 Limitations

Six limitations bound the scope of these results. The band of Sun et al. (2018) was derived for a difference between means and is applied here to a quantile, so that the comparison is one of order of magnitude. The risk of this approximation is one-directional, because a band underestimated for quantiles would make the non-detection even safer. The annual aggregation used in the spatial syntheses is the sum of twelve monthly quantiles and not the quantile of the annual total, and as quantiles are not additive this sum underestimates the annual value, which is also conservative.

The uncertainty partition inherits the limitations of the original framework. Lehner et al. (2020) demonstrated that the Hawkins and Sutton approach works well at the global scale, with a potential methodological bias below 20%, but that at local and regional scales this bias may reach 50% when large initial-condition ensembles are not available. As the present study uses a single member per model, the shares reported here should be read as relative orders of magnitude and not as precise estimates. In the same vein, Pathak et al. (2023) showed that the information contained in 57 CMIP6 models can be explained by about eleven independent models, so that the effective number of degrees of freedom of a five-model ensemble is probably fewer than five.

Three additional restrictions should be considered. The change factor is identical across sources by construction, a condition that allows the observational effect to be isolated in the baseline but prevents testing whether models would respond differently to different bases. The gamma distribution underestimates the upper tail of daily intensity, a limitation that does not affect the results because dependable precipitation is read in the lower tail of the monthly total, but which restricts the use of the same parameters for heavy rainfall purposes. Finally, the network is concentrated in a region of homogeneous climate without a dry season, so that transferring the procedure to regimes with marked seasonality requires a new evaluation of the models, as Silva et al. (2026) recommend in concluding that models should be chosen by their performance in the region of interest.

5 Conclusion

For monthly dependable precipitation in northwestern Rio Grande do Sul, the change projected up to 2070 is not separable from the natural variability of the climate itself. None of the 9504 combinations of site, month and source evaluated crossed the detection threshold, in none of the three scenarios and in neither of the two future windows, and the most favourable case of the whole network reached 0.831 of the threshold. The conclusion depends neither on ensemble composition, since it holds with each model removed in turn, nor on the length of the observed record, since even in the limit of an infinitely long record the detectable fraction would not exceed 1.20%.

The methodological decision of greatest consequence is therefore not which emission pathway to consider, but which observational dataset to adopt as the baseline. The sources evaluated agree on the annual volume and disagree on the daily structure that produces it, and this

disagreement propagates to the lower quantile that planning applies, accounting for about 4.4 times more variance than the emission pathway. For institutions that size irrigation or define sowing windows in the region, the practical result is that methodological effort yields more when directed at the choice and the qualification of the observational base than at the selection of the future scenario. The procedure described here is transferable to any network with a sufficient daily record, and its application in regimes with marked seasonality requires a new local evaluation of the models.

References

Abreu MC, Souza A, Lyra GB, et al (2023) Assessment and characterization of the monthly probabilities of rainfall in Midwest Brazil using different goodness-of-fit tests as probability density functions selection criteria. Theor Appl Climatol 151:491-513. https://doi.org/10.1007/s00704-022-04286-z

Ahmad MJ, Choi K-S (2021) Climate-induced perspective variations in irrigation schedules and design water requirements for the rice-wheat system. Agronomy 11:2006. https://doi.org/10.3390/agronomy11102006

Almazroui M, Ashfaq M, Islam MN, et al (2021) Assessment of CMIP6 performance and projected temperature and precipitation changes over South America. Earth Syst Environ 5:155-183. https://doi.org/10.1007/s41748-021-00233-6

Alvares CA, Stape JL, Sentelhas PC, Gonçalves JLM, Sparovek G (2013) Köppen's climate classification map for Brazil. Meteorologische Zeitschrift 22:711-728. https://doi.org/10.1127/0941-2948/2013/0507

Ávila LF, Mello CR, Viola MR (2009) Mapeamento da precipitação mínima provável para o sul de Minas Gerais. Rev Bras Eng Agríc Ambient 13(supl):906-915. https://doi.org/10.1590/S1415-43662009000700013

Ballarin AS, Wendland E, Zaerpour M, Hatami S, Meira Neto AA, Papalexiou SM (2024) Frequency rather than intensity drives projected changes of rainfall events in Brazil. Earths Future 12:e2023EF004053. https://doi.org/10.1029/2023EF004053

Bandeira WJA, Ziotti JJ, Carvalho IR, Lúcio ADC (2026) Data and code for: Observational source choice outweighs the emission scenario in projected dependable precipitation (northwestern Rio Grande do Sul, Brazil). Zenodo. https://doi.org/10.5281/zenodo.23402577

Beck HE, Vergopolan N, Pan M, Levizzani V, van Dijk AIJM, Weedon GP, Brocca L, Pappenberger F, Huffman GJ, Wood EF (2017) Global-scale evaluation of 22 precipitation datasets using gauge observations and hydrological modeling. Hydrol Earth Syst Sci 21:6201-6217. https://doi.org/10.5194/hess-21-6201-2017

Calegario A, Althoff D, Lourenço A (2026) hydrobr: access to the Brazilian National Water Agency (Agência Nacional de Águas) hydrological data. R package version 0.0.0.9000. https://github.com/hydroversebr/hydrobr

728 Casanueva A, Herrera S, Iturbide M, et al (2020) Testing bias adjustment methods for regional
729 climate change applications under observational uncertainty and resolution mismatch. Atmos Sci
730 Lett 21:e978. https://doi.org/10.1002/asl.978

731 Chen J, Brissette FP (2014) Stochastic generation of daily precipitation amounts: review and
732 evaluation of different models. Clim Res 59:189-206. https://doi.org/10.3354/cr01214

733 Chow VT (1964) Handbook of applied hydrology. McGraw-Hill, New York

734 Coan BP, Back ÁJ, Bonetti AV (2014) Precipitação mensal e anual provável no estado de Santa
735 Catarina. Rev Bras Climatol 15:122-142. https://doi.org/10.5380/abclima.v15i0.38348

736 Delignette-Muller ML, Dutang C (2015) fitdistrplus: an R package for fitting distributions. J Stat
737 Softw 64(4):1-34. https://doi.org/10.18637/jss.v064.i04

738 Deser C, Phillips A, Bourdette V, Teng H (2012) Uncertainty in climate change projections: the
739 role of internal variability. Clim Dyn 38:527-546. https://doi.org/10.1007/s00382-010-0977-x

740 Duarte YCN, Sentelhas PC (2020) NASA/POWER and DailyGridded weather datasets: how good
741 they are for estimating maize yields in Brazil? Int J Biometeorol 64:319-329.
742 https://doi.org/10.1007/s00484-019-01810-1

743 Ferreira GWS, Reboita MS, Ribeiro JGM, Souza CA (2023) Assessment of precipitation and
744 hydrological droughts in South America through statistically downscaled CMIP6 projections.
745 Climate 11:166. https://doi.org/10.3390/cli11080166

746 Firpo MÂF, Guimarães BS, Dantas LG, Silva MGB, Alves LM, Chadwick R, Llopart M, Oliveira
747 GS (2022) Assessment of CMIP6 models' performance in simulating present-day climate in Brazil.
748 Front Clim 4:948499. https://doi.org/10.3389/fclim.2022.948499

749 Funk C, Peterson P, Landsfeld M, Pedreros D, Verdin J, Shukla S, Husak G, Rowland J, Harrison
750 L, Hoell A, Michaelsen J (2015) The climate hazards infrared precipitation with stations: a new
751 environmental record for monitoring extremes. Sci Data 2:150066.
752 https://doi.org/10.1038/sdata.2015.66

753 Gabriel KR, Neumann J (1962) A Markov chain model for daily rainfall occurrence at Tel Aviv. Q
754 J R Meteorol Soc 88:90-95. https://doi.org/10.1002/qj.49708837511

755 Gampe D, Schmid J, Ludwig R (2019) Impact of reference dataset selection on RCM evaluation,
756 bias correction, and resulting climate change signals of precipitation. J Hydrometeorol 20:1813-
757 1828. https://doi.org/10.1175/JHM-D-18-0108.1

758 Gampe D, Schwingshackl C, Böhnisch A, Mittermeier M, Sandstad M, Wood RR (2024) Applying
759 global warming levels of emergence to highlight the increasing population exposure to temperature
760 and precipitation extremes. Earth Syst Dyn 15:589-605. https://doi.org/10.5194/esd-15-589-2024

761 García-Franco JL, Gray LJ, Osprey S (2020) The American monsoon system in HadGEM3 and
762 UKESM1. Weather Clim Dyn 1:349-371. https://doi.org/10.5194/wcd-1-349-2020

763 Gumbel EJ (1958) Statistics of extremes. Columbia University Press, New York

764 Gupta HV, Kling H, Yilmaz KK, Martinez GF (2009) Decomposition of the mean squared error
765 and NSE performance criteria: implications for improving hydrological modelling. J Hydrol
766 377:80-91. https://doi.org/10.1016/j.jhydrol.2009.08.003

767 Hawkins E, Sutton R (2009) The potential to narrow uncertainty in regional climate predictions.
768 Bull Am Meteorol Soc 90:1095-1108. https://doi.org/10.1175/2009BAMS2607.1

769 Katz RW (1977) Precipitation as a chain-dependent process. J Appl Meteorol 16:671-676.
770 https://doi.org/10.1175/1520-0450(1977)016<0671:PAACDP>2.0.CO;2

771 Kazora J, Zhu W, Oo KT, Akimana D, Kalisa JP, Ayugi BO, Gahigi A (2025) Evaluation of CMIP6
772 models for rainfall simulation in Central Eastern Africa using extreme precipitation indices. Discov
773 Atmos 3:40. https://doi.org/10.1007/s44292-025-00066-2

774 Lehner F, Deser C, Maher N, et al (2020) Partitioning climate projection uncertainty with multiple
775 large ensembles and CMIP5/6. Earth Syst Dyn 11:491-508. https://doi.org/10.5194/esd-11-491-
776 2020

777 Mandal KG, Padhi J, Kumar A, et al (2015) Analyses of rainfall using probability distribution and
778 Markov chain models for crop planning in Daspalla region in Odisha, India. Theor Appl Climatol
779 121:517-528. https://doi.org/10.1007/s00704-014-1259-z

780 Maraun D, Shepherd TG, Widmann M, Zappa G, Walton D, Gutiérrez JM, Hagemann S, Richter I,
781 Soares PMM, Hall A, Mearns LO (2017) Towards process-informed bias correction of climate
782 change simulations. Nat Clim Change 7:764-773. https://doi.org/10.1038/nclimate3418

783 Martel J-L, Mailhot A, Brissette F, Caya D (2018) Role of natural climate variability in the
784 detection of anthropogenic climate change signal for mean and extreme precipitation at local and
785 regional scales. J Clim 31:4241-4263. https://doi.org/10.1175/JCLI-D-17-0282.1

786 Monteiro LA, Sentelhas PC, Pedra GU (2018) Assessment of NASA/POWER satellite-based
787 weather system for Brazilian conditions and its impact on sugarcane yield simulation. Int J Climatol
788 38:1571-1581. https://doi.org/10.1002/joc.5282

789 Nogueira SMC, Moreira MA, Volpato MML (2018) Evaluating precipitation estimates from Eta,
790 TRMM and CHIRPS data in the south-southeast region of Minas Gerais state, Brazil. Remote Sens
791 10:313. https://doi.org/10.3390/rs10020313

792 Pannak M, Sittichok K, Thepprasit C, Chompuchan C (2026) Spatial exceedance probability
793 mapping of monthly rainfall using gridded precipitation products in an orographically complex
794 monsoon basin, western Thailand. Hydrology 13:155. https://doi.org/10.3390/hydrology13060155

795 Paredes-Trejo FJ, Barbosa HA, Lakshmi Kumar TV (2017) Validating CHIRPS-based satellite
796 precipitation estimates in Northeast Brazil. J Arid Environ 139:26-40.
797 https://doi.org/10.1016/j.jaridenv.2016.12.009

798 Parkes B, Higginbottom TP, Hufkens K, Ceballos F, Kramer B, Foster T (2019) Weather dataset
799 choice introduces uncertainty to estimates of crop yield responses to climate variability and change.
800 Environ Res Lett 14:124089. https://doi.org/10.1088/1748-9326/ab5ebb

801 Pathak R, Dasari HP, Ashok K, Hoteit I (2023) Effects of multi-observations uncertainty and
802 models similarity on climate change projections. npj Clim Atmos Sci 6:144.
803 https://doi.org/10.1038/s41612-023-00473-5

804 Pendergrass AG, Knutti R (2018) The uneven nature of daily precipitation and its change. Geophys
805 Res Lett 45:11980-11988. https://doi.org/10.1029/2018GL080298

806 Pohlert T (2026) trend: non-parametric trend tests and change-point detection. R package version
807 1.1.8. https://doi.org/10.32614/CRAN.package.trend

808 Prasetya R, Djuhana D, Saputro AH, Permana DS (2026) Evaluation and ranking of NEX-GDDP-
809 CMIP6 models based on monthly precipitation climatology over Indonesia. Front Clim 8:1748663.
810 https://doi.org/10.3389/fclim.2026.1748663

811 Prein AF, Gobiet A (2017) Impacts of uncertainties in European gridded precipitation observations
812 on regional climate analysis. Int J Climatol 37:305-327. https://doi.org/10.1002/joc.4706

813 Reboita MS, Ferreira GWS, Ribeiro JGM, Ali S (2024) Assessment of precipitation and near-
814 surface temperature simulation by CMIP6 models in South America. Environ Res Clim 3:025011.
815 https://doi.org/10.1088/2752-5295/ad3fdb

816 Salio P, Hobouchian MP, García Skabar Y, Vila D (2015) Evaluation of high-resolution satellite
817 precipitation estimates over southern South America using a dense rain gauge network. Atmos Res
818 163:146-161. https://doi.org/10.1016/j.atmosres.2014.11.017

819 Samset BH, Fuglestvedt JS, Lund MT (2020) Delayed emergence of a global temperature response
820 after emission mitigation. Nat Commun 11:3261. https://doi.org/10.1038/s41467-020-17001-1

821 Silva JC, Heldwein AB, Martins FB, Trentin G, Grimm EL (2007) Análise de distribuição de chuva
822 para Santa Maria, RS. Rev Bras Eng Agríc Ambient 11:67-72. https://doi.org/10.1590/S1415-
823 43662007000100009

824 Silva JRS, Taveira MK, Serrano ROP, Mesquita AA, Moreira JGV (2021) Probability of rainfall
825 for the city of Cruzeiro do Sul, Acre, Brazil. Rev Ambient Água 16:e2593.
826 https://doi.org/10.4136/ambi-agua.2593

827 Silva ML, Reboita MS, Barreto NJC, Alves LM (2026) Assessment of CMIP6 models'
828 performance for South America: multilevel perspective. Theor Appl Climatol 157:683.
829 https://doi.org/10.1007/s00704-026-06585-1

830 Sparks AH (2018) nasapower: a NASA POWER global meteorology, surface solar energy and
831 climatology data client for R. J Open Source Softw 3:1035. https://doi.org/10.21105/joss.01035

832 Sun F, Roderick ML, Farquhar GD (2018) Rainfall statistics, stationarity, and climate change. Proc
833 Natl Acad Sci USA 115:2305-2310. https://doi.org/10.1073/pnas.1705349115

834 Talukder A, Shahid S, Hwang S, Alam E, Islam MK, Kamruzzaman M (2025) Optimizing the
835 multi-model ensemble of CMIP6 GCMs for climate simulation over Bangladesh. Sci Rep
836 15:11343. https://doi.org/10.1038/s41598-025-96446-0

837 Tarek M, Brissette F, Arsenault R (2021) Uncertainty of gridded precipitation and temperature
838 reference datasets in climate change impact studies. Hydrol Earth Syst Sci 25:3331-3350.
839 https://doi.org/10.5194/hess-25-3331-2021

840 Thom HCS (1958) A note on the gamma distribution. Mon Weather Rev 86:117-122.
841 https://doi.org/10.1175/1520-0493(1958)086<0117:ANOTGD>2.0.CO;2

842 Thrasher B, Wang W, Michaelis A, Melton F, Lee T, Nemani R (2022) NASA Global Daily
843 Downscaled Projections, CMIP6. Sci Data 9:262. https://doi.org/10.1038/s41597-022-01393-4

844 Ucar Y, Kocięcka J, Liberacki D, Rolbiecki R (2023) Analysis of crop water requirements for apple
845 using dependable rainfall. Atmosphere 14:99. https://doi.org/10.3390/atmos14010099

Verdin A, Rajagopalan B, Kleiber W, Podestá G, Bert F (2018) A conditional stochastic weather generator for seasonal to multi-decadal simulations. J Hydrol 556:835-846. https://doi.org/10.1016/j.jhydrol.2015.12.036

Wilks DS (1992) Adapting stochastic weather generation algorithms for climate change studies. Clim Change 22:67-84. https://doi.org/10.1007/BF00143344

Willmott CJ (1981) On the validation of models. Phys Geogr 2:184-194. https://doi.org/10.1080/02723646.1981.10642213

Wilson Kemsley S, Osborn TJ, Dorling SR, Wallace C, Parker JB (2021) Selecting Markov chain orders for generating daily precipitation series across different Köppen climate regimes. Int J Climatol 41:6223-6237. https://doi.org/10.1002/joc.7175

Yoo S-H, Choi J-Y, Nam W-H, Hong E (2012) Analysis of design water requirement of paddy rice using frequency analysis affected by climate change in South Korea. Agric Water Manag 112:33-42. https://doi.org/10.1016/j.agwat.2012.06.002

Statements and Declarations

Funding The authors declare that no funds, grants or other support were received during the preparation of this manuscript.

Competing interests The authors declare no competing interests.

Ethics approval Not applicable.

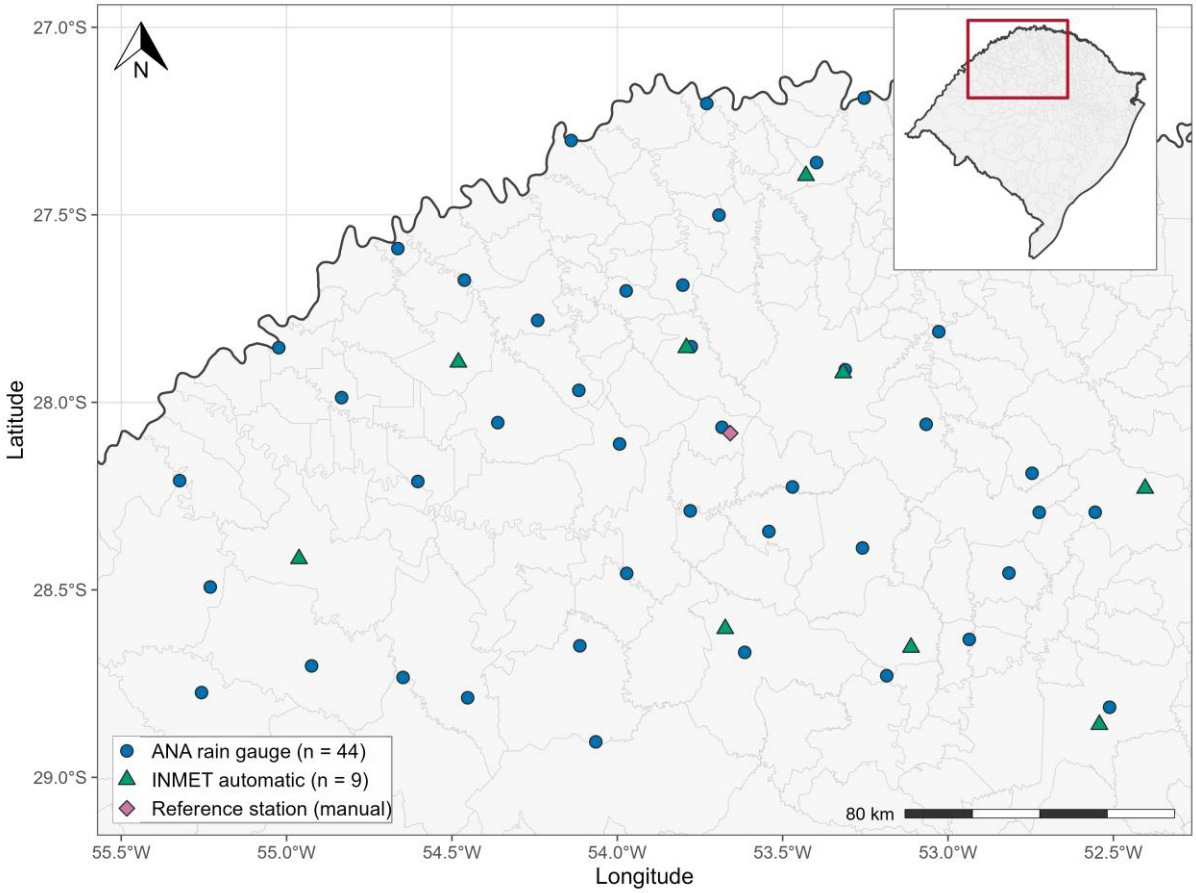
Consent to participate and consent for publication Not applicable.

Data availability The observational series, the NEX-GDDP-CMIP6 point extract and the derived datasets are openly available in Zenodo at https://doi.org/10.5281/zenodo.23402577, in the same repository as the analysis code. The primary data are public and were obtained from ANA/HidroWeb, INMET, CHIRPS v2.0, NASA POWER and NEX-GDDP-CMIP6, as described in Section 2.2. The daily record of the reference rain gauge, which is privately operated by one of the authors, is included in the deposit. The repository holds the precipitation values extracted at the network cells rather than the original NEX-GDDP-CMIP6 fields, which allows the whole analysis to be reproduced without downloading them.

Code availability The analysis scripts are deposited together with the data in the same repository, at https://doi.org/10.5281/zenodo.23402577. The deposit reproduces every table and figure of this article from the files it contains, with no external download.

Author contributions WJAB: conceptualisation, data curation, formal analysis, software, visualisation, writing of the original draft. JJZ: data acquisition, investigation. IRC: supervision, methodology, writing (review and editing). ADL: supervision, methodology, validation, writing (review and editing).

Use of generative artificial intelligence The authors used a large language model to assist with language editing and with the organisation of the manuscript. The authors reviewed and edited all content and take full responsibility for the published article.



885
886 **Fig. 1** Study area and monitoring network in northwestern Rio Grande do Sul, Brazil. Circles
887 denote the 44 ANA rain gauge sites retained after quality control, triangles the nine INMET
888 automatic stations located less than 30 km from a network site, and the diamond the reference rain
889 gauge, read manually each day, 3.0 km from ANA site 2853035. The inset shows the location within
890 Rio Grande do Sul

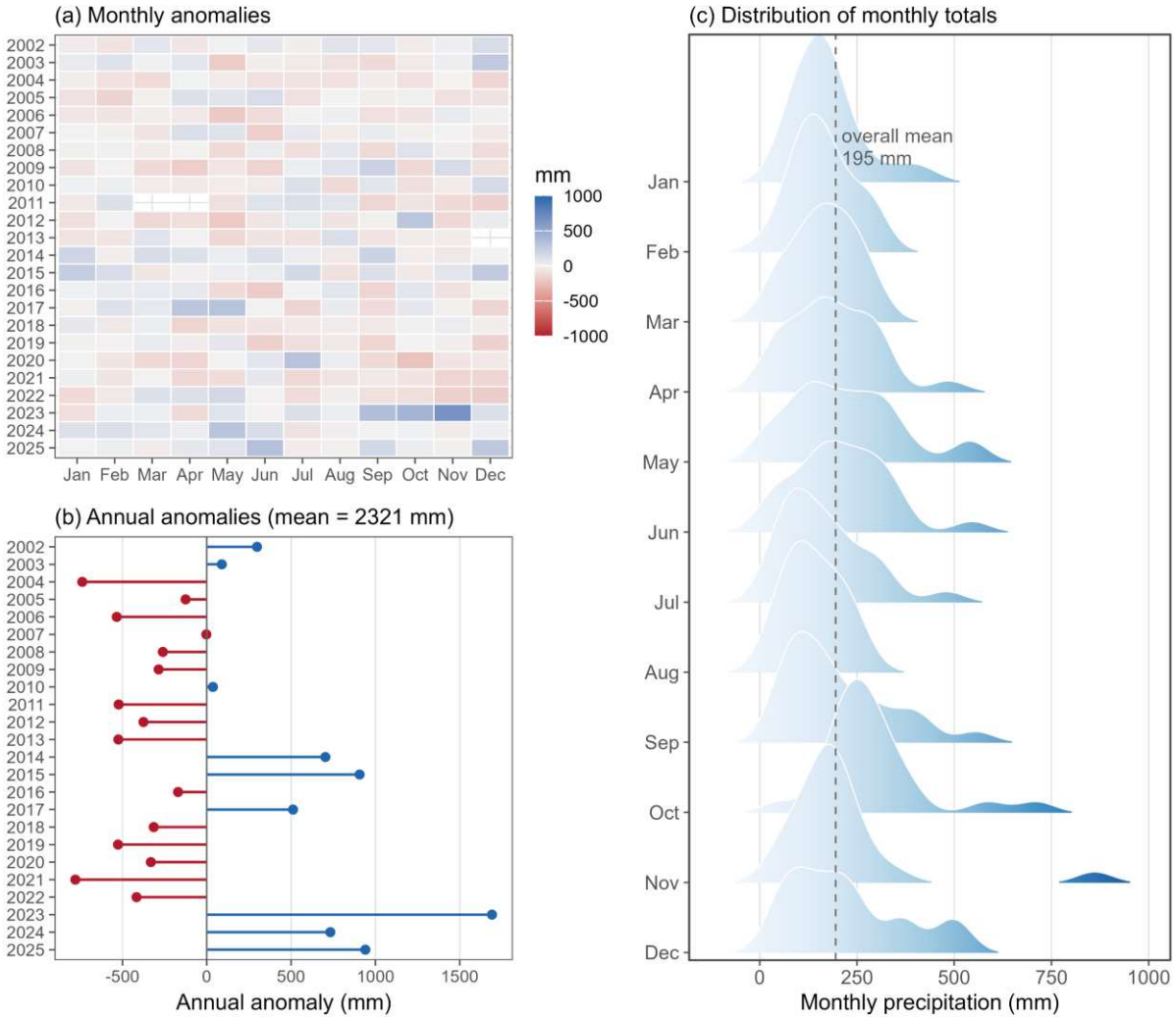


Fig. 2 Characterization of the baseline at the reference rain gauge, 2002 to 2025. (a) Monthly anomalies relative to the monthly means of the 24 years, with white cells denoting the months excluded because of documented collection failure, March and April 2011 and December 2013. (b) Annual anomalies relative to the mean of the series. (c) Distribution of monthly totals, with the dashed line marking the overall monthly mean

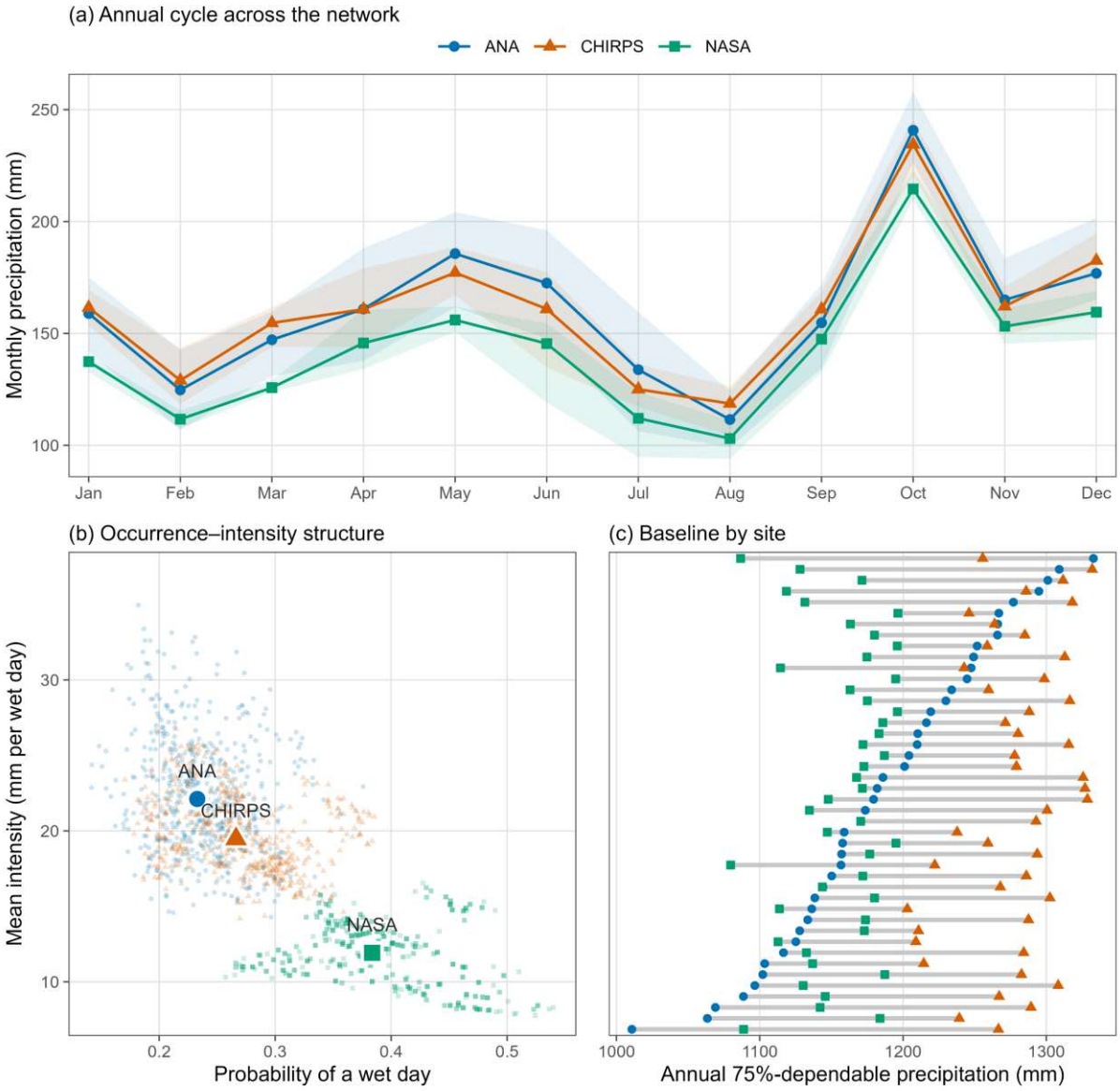


Fig. 3 Disagreement among the observational sources at the same locations. (a) Annual cycle over the network, with the band spanning the 10th to the 90th percentile across sites. (b) Occurrence-intensity structure, in which small symbols represent individual site-month combinations and large symbols the median of each source. (c) Annual 75% dependable precipitation per site, with sites ordered by the value of the ANA network, for which the median spread among sources is 11.9%

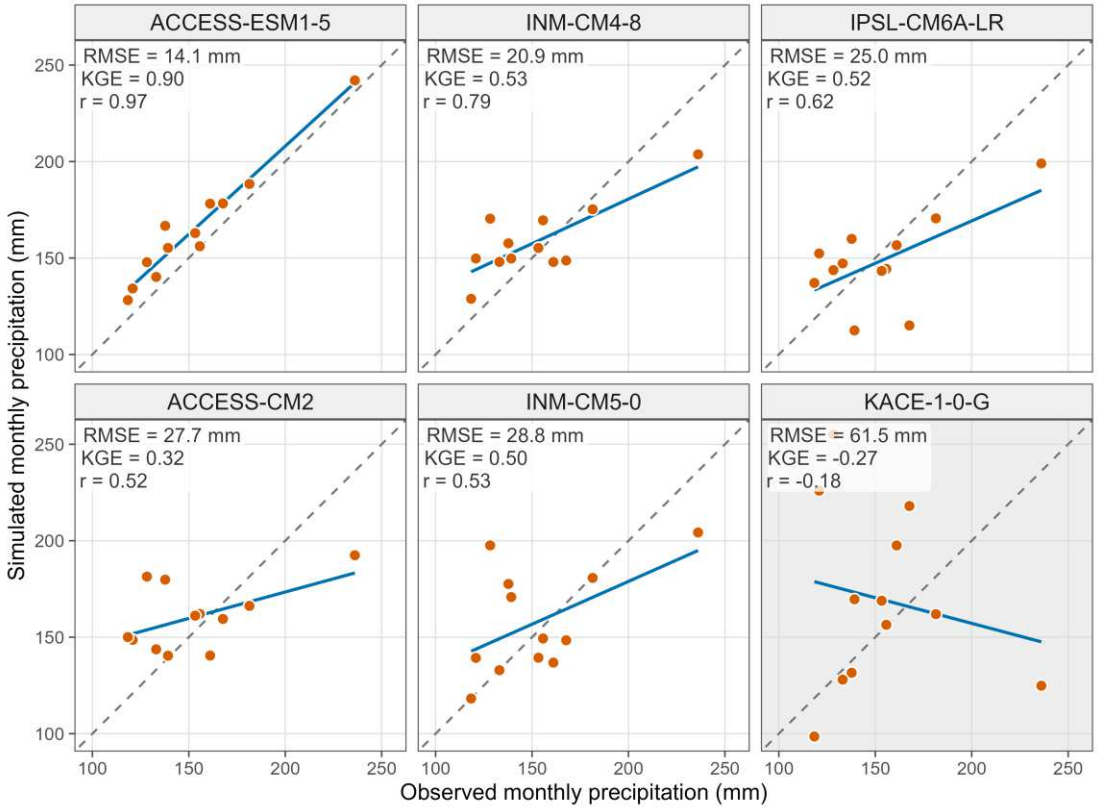


Fig. 4 Simulated against observed monthly climatology for the six NEX-GDDP-CMIP6 models in the historical period, 2002 to 2014. The reference is the 44-site ANA network. The dashed line denotes the 1:1 relation and the solid line the linear fit. Panels are ordered by RMSE and the shaded panel marks the model excluded from the ensemble

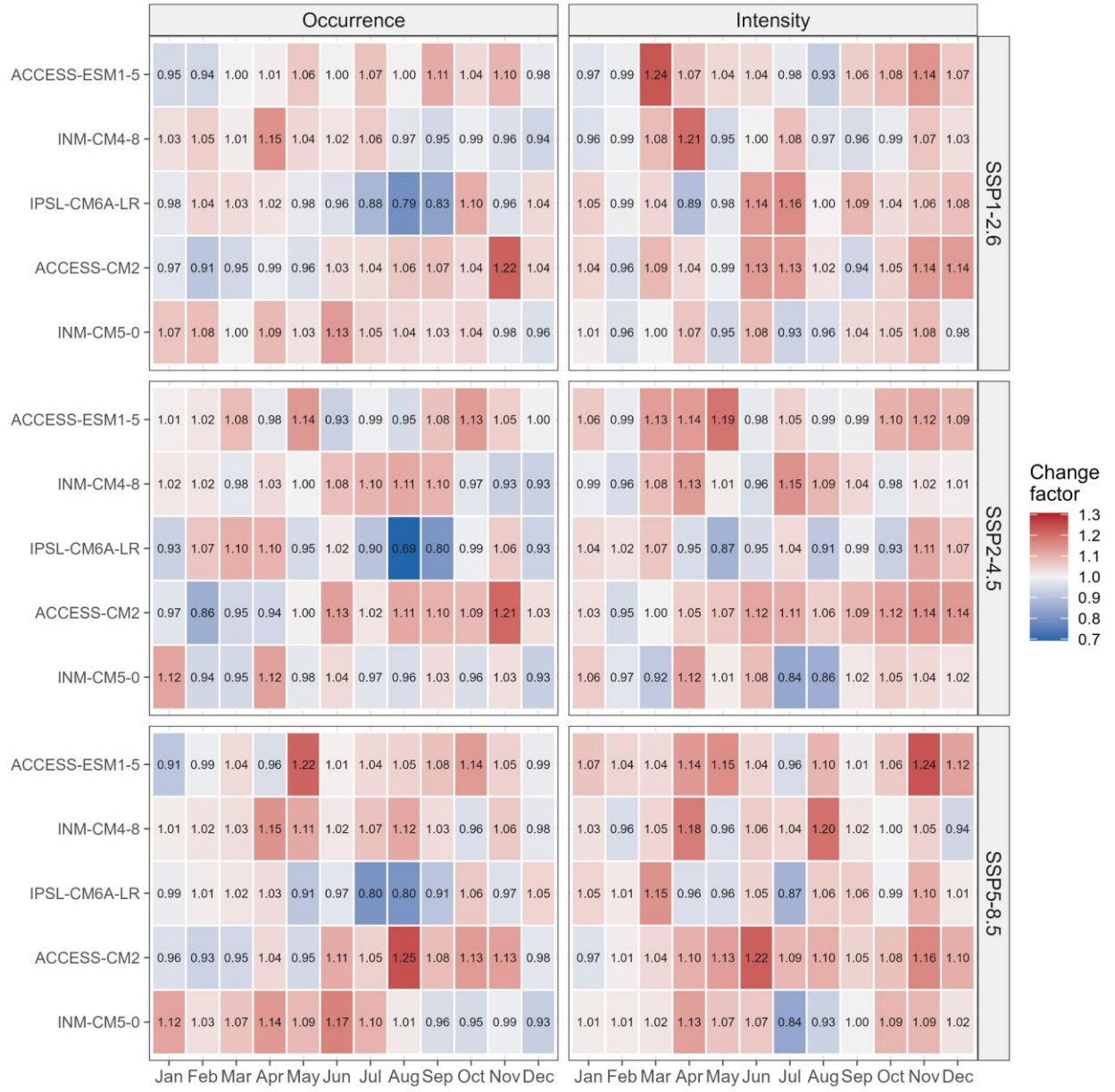


Fig. 5 Monthly change factors of rainfall occurrence and intensity, by model and emission scenario, for the 2041 to 2070 window. Values are medians across the 44 network sites and are expressed relative to the historical window of 1985 to 2014, so that values above 1 denote an increase. The 2027 to 2040 window is given in Online Resource 1, Section S3

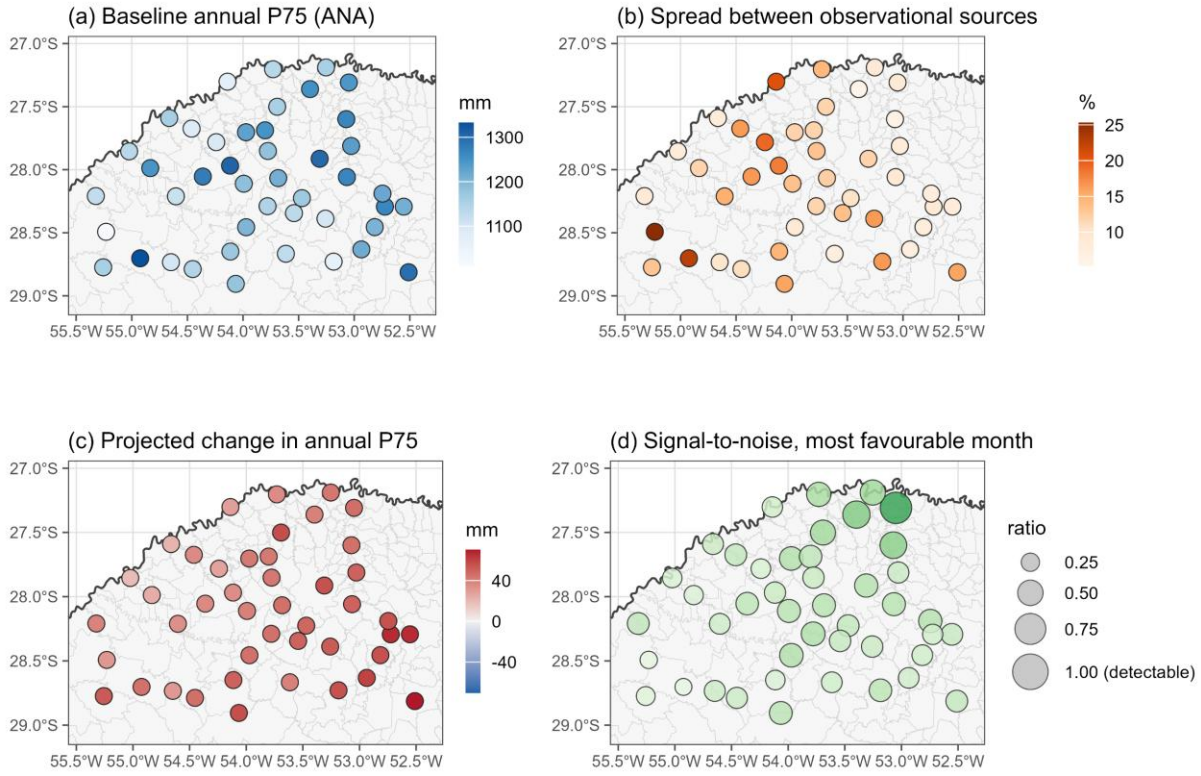


Fig. 6 Spatial synthesis for the SSP2-4.5 scenario and the 2041 to 2070 window. (a) Baseline of annual 75% dependable precipitation in the ANA network, obtained as the sum of the twelve monthly values. (b) Relative range among ANA, CHIRPS and NASA POWER at the same site. (c) Projected change in the same annual quantity. (d) Signal-to-noise ratio, defined as the absolute projected change divided by the natural variability band, taken at each site in the month of highest ratio. The scale is capped at 1.0, which is the detectability threshold, reached by no site, the network maximum being 0.77

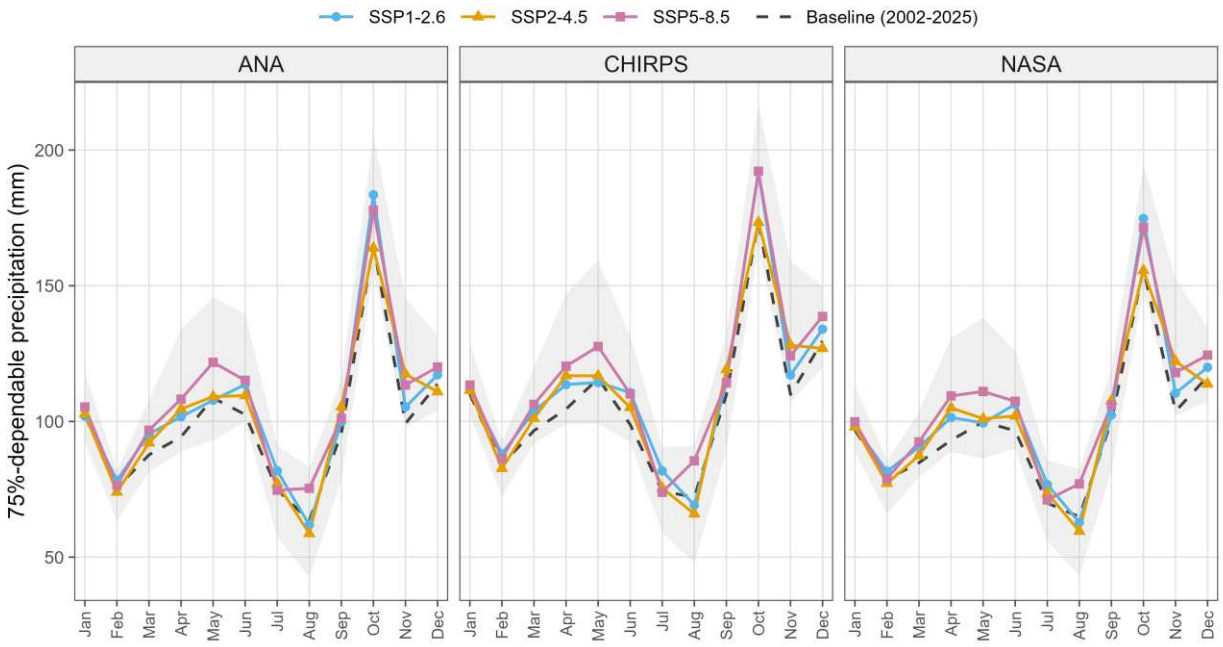


Fig. 7 Monthly 75% dependable precipitation, baseline and projected, for each observational source, in the 2041 to 2070 window. The baseline, in dashed grey, does not depend on the emission scenario and is therefore shown once. The coloured lines correspond to the three scenarios and are medians across the 44 network sites. The grey band is the range among the five retained models, taken as the median across sites and pooled over the three scenarios, and not a confidence interval

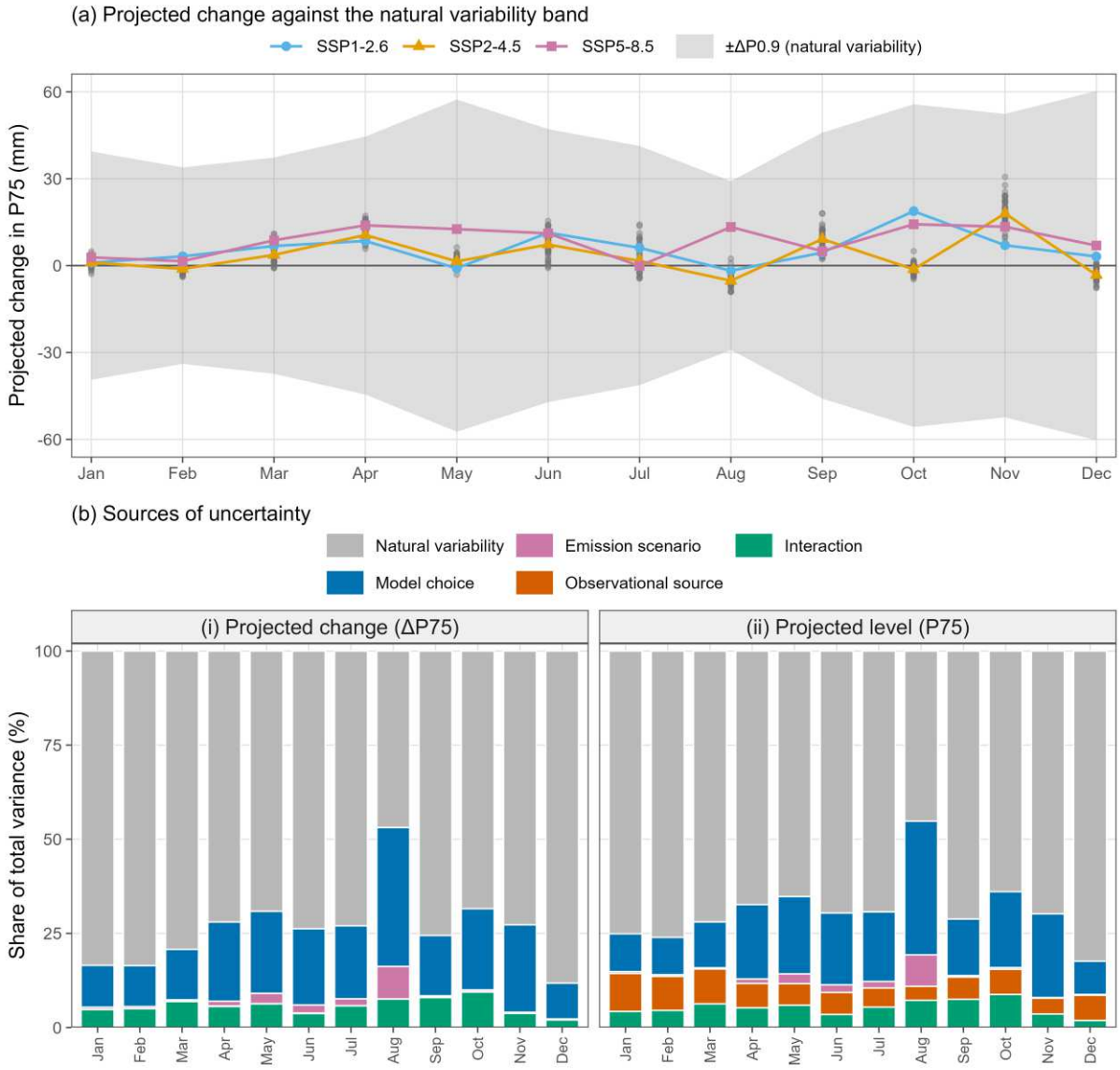


Fig. 8 Detectability of the projected signal in the 2041 to 2070 window. (a) Projected change in 75% dependable precipitation confronted with the natural variability band. The band depends only on the interannual standard deviation and on the lengths of the windows, so that it is identical across scenarios and appears once. The coloured lines are the network medians for the three scenarios and the grey points are the 44 sites under SSP2-4.5, with the ANA baseline and a median ratio of 0.088. (b) Partition of the total variance for the projected change and for the projected level. Components are means across the 44 sites, so that each bar sums to 100%

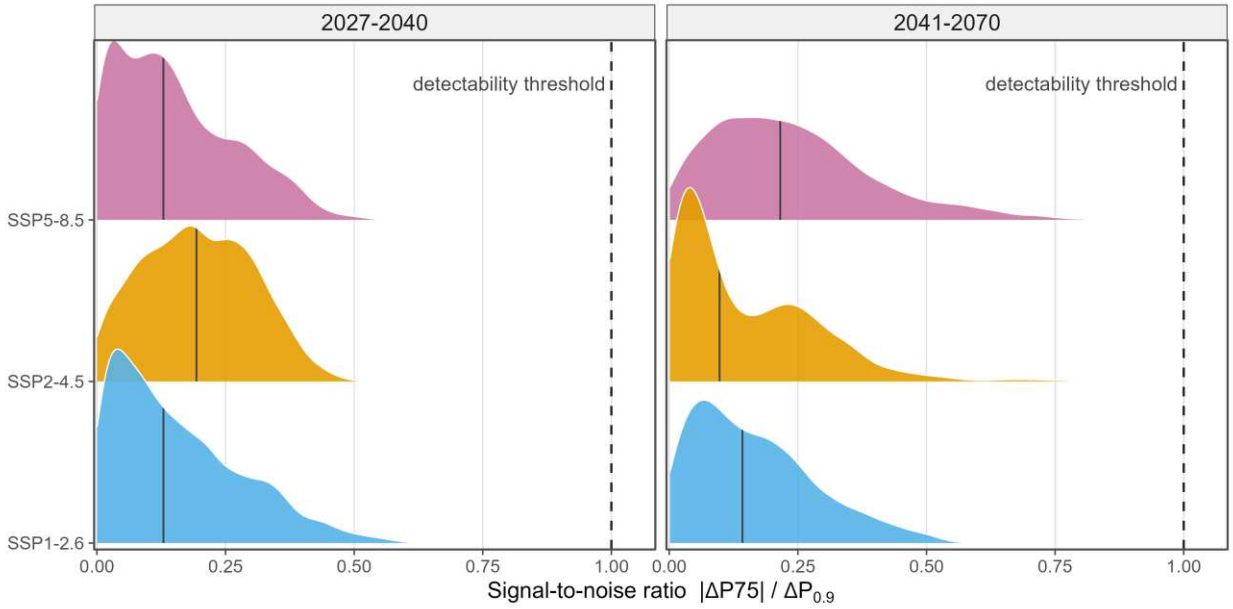


Fig. 9 Distribution of the signal-to-noise ratio, defined as the absolute projected change in 75% dependable precipitation divided by the natural variability band, over all combinations of site, month and source. The inner vertical lines mark the median of each distribution and the dashed line marks unit ratio, which is the detectability threshold. No combination reaches it in any scenario or window, 0.831 being the largest value of the whole analysis

Table 1. Descriptive statistics of the observed series, by source, after quality control

Source	n	Yrs	Total	SD	CV	WD	Ī	P95	P99	Trend	Break
ANA	44	21	1934	428	22.1	23.8	22.3	68.5	107.3	4/44	1/44
CHIRPS	44	24	1920	379	19.7	26.8	19.6	52.9	77.1	0/44	0/44
NASA	44	24	1704	338	19.8	38.9	11.8	38.8	61.1	0/44	0/44
INMET	9	15	1865	353	18.9	28.4	17.8	57.6	92.2	0/6	0/6
Ref. gauge	1	23	2343	627	26.8	26.1	24.6	77.1	122.6	0/1	0/1

Sources are the ANA rain-gauge network, CHIRPS v2.0, NASA POWER, the INMET automatic stations and the private reference gauge. All series cover 2002 to 2025. n is the number of sites and Yrs the median number of usable years per site. Total is the mean annual total and SD its standard deviation, both in mm. CV is the coefficient of variation of the annual total, in %. WD is the share of wet days, in %, and Ī the mean depth on those days, in mm. P95 and P99 are percentiles of wet-day depth, in mm. A wet day is a day with a total of at least 1.0 mm. A month enters the analysis with at least 26 valid days and a year with at least 90% of the days. Ī, P95 and P99 refer to wet-day depths and not to all days. Trend and Break give the number of series flagged over the number tested, by the Mann-Kendall test and the Pettitt test respectively, both at $p < 0.05$, with about 5% of positives expected by chance in the number of series tested. The denominator of those two columns is the number of series with at least ten usable years, smaller than the number of sites in the case of the INMET automatic stations. One ANA site, 2854016, was excluded for disagreeing with its neighbours, with a median r of 0.63 against the seven sites less than 50 km away, a Pettitt change point at $p = 0.005$ and a Sen slope of -52 mm per year.

Table 2. Monthly parameters of the occurrence-intensity model in the ANA network

Month	p01	p11	π	p11 – p01	ΔAIC	α	β	Ī (mm)	Wet days
Jan	0.22	0.40	0.267	0.186	46.3	1.108	0.0566	19.6	178
Feb	0.21	0.36	0.245	0.155	36.0	1.129	0.0657	17.2	148
Mar	0.18	0.40	0.227	0.225	53.3	1.133	0.0537	21.1	151
Apr	0.18	0.34	0.214	0.158	35.3	1.037	0.0417	24.9	138
May	0.18	0.44	0.245	0.254	65.5	0.954	0.0381	25.0	164
Jun	0.18	0.42	0.24	0.242	56.7	1.055	0.0454	23.2	156
Jul	0.16	0.37	0.205	0.213	46.8	1.085	0.0529	20.5	136
Aug	0.16	0.34	0.192	0.184	34.0	1.155	0.0621	18.6	130
Sep	0.20	0.40	0.247	0.197	41.5	1.139	0.0556	20.5	156
Oct	0.25	0.40	0.297	0.146	40.5	1.202	0.0467	25.7	193
Nov	0.19	0.35	0.227	0.162	40.2	1.174	0.0479	24.5	146
Dec	0.21	0.38	0.253	0.167	39.0	1.100	0.0491	22.4	165

Values are medians across the 44 network sites. The quantities p01 and p11 are the transition probabilities of the first-order Markov chain and π is the marginal probability of a wet day implied by the chain, according to Eq. (2). The shape α and the rate β are those of the gamma distribution of Eq. (3) and Ī is the mean wet-day intensity. A positive ΔAIC, the AIC of the independent Bernoulli model minus that of the chain, favours the Markov chain over the Bernoulli model, which occurs in all 1704 combinations of site, source and month. Wet days refer to the whole record and not to a single year.

965 Table 3. Occurrence-intensity structure by observational source

Source	p01	p11	π	p11 – p01	α	Ī (mm)	ΔAIC
ANA rain gauges	0.19	0.38	0.234	0.193	1.102	21.7	42.6
CHIRPS	0.20	0.45	0.264	0.250	1.727	19.5	62.0
NASA POWER	0.24	0.61	0.385	0.371	1.082	12.1	119.0
INMET automatic	0.21	0.45	0.281	0.238	0.969	17.5	41.9
Reference gauge	0.21	0.39	0.259	0.180	0.963	26.7	46.4

966 Values are medians across the sites of each source. Aggregated to the year, the spread among the
967 three sources present at all locations reaches 11.9% of 75% dependable precipitation, as a median
968 across the 44 sites, ranging from 5.3% to 25.3% depending on the location. Symbols are as defined
969 in Table 2.

Table 4. Performance of the six NEX-GDDP-CMIP6 models in the historical period

Model	RMSE (mm)	Bias (mm)	Bias (%)	d	NSE	r	KGE	Ensemble
ACCESS-ESM1-5	14.1	12.1	7.9	0.948	0.80	0.974	0.895	retained
INM-CM4-8	20.9	6.0	3.9	0.820	0.55	0.794	0.532	retained
IPSL-CM6A-LR	25.0	-4.3	-2.8	0.757	0.36	0.620	0.520	retained
ACCESS-CM2	27.7	7.7	5.1	0.657	0.21	0.522	0.324	retained
INM-CM5-0	28.8	5.2	3.4	0.741	0.15	0.526	0.500	retained
KACE-1-0-G	61.5	17.0	11.1	0.275	-2.89	-0.185	-0.267	excluded

The reference is the annual cycle of the 44-site ANA network from 2002 to 2014, the overlap period between the CMIP6 historical simulation and the observational network. Models are ordered by RMSE and d is Willmott's index of agreement. A zero NSE corresponds to the performance of using the observed mean, and negative values denote performance below that reference. KACE-1-0-G was excluded from the ensemble because of a phase error, since the change factor method removes a level bias but does not correct an inverted cycle.

977 Table 5. Projected 75% dependable precipitation and detectability, by month

Month	P75 base (mm)	P75 proj (mm)	Model range (mm)	Change (mm)	ΔP0.9 (mm)	S/N	Agreement
Jan	102.2	102.8	95.5–123.2	1.0	39.4	0.034	0.6
Feb	75.6	74.0	58.9–85.1	-1.1	33.9	0.034	0.6
Mar	87.7	92.1	74.3–111.3	3.7	37.3	0.099	0.6
Apr	94.3	104.6	90.3–125.2	10.6	44.5	0.238	0.8
May	108.6	109.2	89.4–154.4	1.5	57.4	0.028	0.6
Jun	102.6	109.5	91–135.5	7.3	47.1	0.154	0.6
Jul	74.8	77.1	60.8–97.8	1.6	41.3	0.064	0.6
Aug	63.5	58.7	33–82.3	-5.2	29.1	0.180	0.6
Sep	95.6	105.4	69.1–118.7	9.2	45.9	0.200	0.8
Oct	165.3	163.9	151.2–214.9	-1.3	55.7	0.027	0.6
Nov	99.2	117.4	92.3–146.8	18.0	52.4	0.343	0.8
Dec	113.8	111.0	102.8–135.5	-3.2	60.3	0.054	0.6

978 ANA network baseline, SSP2-4.5 scenario, 2041 to 2070 window. Values are medians across the
979 44 sites. Model range is the range between the lowest and the highest value projected by the five
980 retained models, and not a confidence interval. ΔP0.9 is the natural variability band of Eq. (10) and
981 S/N the signal-to-noise ratio of Eq. (11). Agreement is the fraction of ensemble members that agree
982 on the sign of the change. All twelve months were classified as within natural variability. The band
983 was derived for a difference of means and is compared here with a quantile, so that the comparison
984 is one of order of magnitude.

Table 6. Partition of the total variance of the projected quantities

Quantity	Natural (%)	Model (%)	Scenario (%)	Source (%)	Interaction (%)
ΔP75, 2027-2040	77.62	13.20	1.91	0.06	7.21
ΔP75, 2041-2070	73.82	18.76	1.59	0.10	5.72
P75, 2027-2040	74.10	12.67	1.82	4.52	6.88
P75, 2041-2070	68.91	17.66	1.51	6.57	5.35

Components are means across the 44 network sites, so that each row sums to 100%. ΔP75 denotes the projected change and P75 the projected level. Partition after Hawkins and Sutton (2009), extended with a fourth axis, the observational source that defines the baseline. The future window does not enter as a factor because the two windows have different lengths and therefore different natural variability bands, so that the partition was computed separately within each one. The model, scenario and interaction terms are identical for the projected change and for the projected level, because the two quantities differ only by the baseline, which depends on the source alone.

Table 7. Signal-to-noise ratio and detectability, by emission scenario and future window

Window	Scenario	Cases	|ΔP75| (mm)	ΔP0.9 (mm)	S/N median	S/N P90	S/N max	Factor	Detectable (%)
2027-2040	SSP1-2.6	1584	6.2	48.6	0.129	0.340	0.578	7.8	0
2027-2040	SSP2-4.5	1584	8.7	48.6	0.193	0.337	0.725	5.6	0
2027-2040	SSP5-8.5	1584	5.7	48.6	0.129	0.320	0.518	8.5	0
2041-2070	SSP1-2.6	1584	5.2	39.8	0.142	0.335	0.570	7.6	0
2041-2070	SSP2-4.5	1584	3.8	39.8	0.098	0.329	0.772	10.5	0
2041-2070	SSP5-8.5	1584	8.8	39.8	0.216	0.446	0.831	4.5	0

Cases are all combinations of site, month and observational source with a usable natural variability band, restricted to ANA, CHIRPS and NASA POWER. S/N is the signal-to-noise ratio of Eq. (11), given as the median, the 90th percentile and the maximum over the cases. Factor is the band ΔP0.9 divided by the absolute projected change, that is, how many times larger the signal would have to be to cross the threshold. Factor and the median S/N are computed independently, so that one is not the exact inverse of the other. No case was classified as detectable in any scenario or window.

Supplementary Files

This is a list of supplementary files associated with this preprint. Click to download.

- ESM1.pdf